

Hybrid Eulerian-Lagrangian Topology Optimization

Yue Li

A Thesis

in

Department of Engineering and Applied Science

For the Graduate Group in Computer Graphics and Game Technology

Presented to the Faculties of the University of Pennsylvania

in

Partial Fulfillment of the Requirements for the

Degree of Master of Science in Engineering

2019

Supervisor of Thesis

Chenfanfu Jiang, Assistant Professor

Graduate Group Chairperson

Stephen H. Lane, Professor of Practice

Hybrid Eulerian-Lagrangian Topology Optimization

© COPYRIGHT

2019

Yue Li

ACKNOWLEDGEMENT

My most sincere gratitude goes to my advisor Dr. Chenfanfu Jiang at the University of Pennsylvania. This thesis can not be materialized without guidance and support from him for the last six months. Dr. Jiang offered great help in deciding the research directions whenever experiments went against expectations. I can not imagine how many detours I have to take without his expertise in physics-based simulation and optimization.

Pertaining to the accomplishment of this thesis and important guidance in employing numerical optimization methods, I would like to thank Minchen Li, Ph.D. at the University of Pennsylvania and Xuan Li, visiting scholar at the University of Pennsylvania for their great help in providing crucial support and sharp insights in my research process. I would also like to thank Dr. Bo Zhu at Dartmouth College for his insights and guidance in topology optimization.

I would like to heartily thank Dr. Stephen Lane, Director of the Computer Graphics and Game Technology program at the University of Pennsylvania, for his support and guidance in helping me to be a successful master candidate in the Computer Graphics and Game Technology program. The demanding and mind-opening courses selected by Dr. Lane made me well-prepared in conducting research and sparked my great interest and determination in devoting my passion for computer graphics.

I am especially grateful for the endorsement and recommendation for me to pursue a Doctor's degree from Dr. Jiang and Dr. Norman Badler, Rachleff Professor at the University of Pennsylvania.

Last but by no means least, I would like to acknowledge my fellow CGGT master students and all the excellent Ph.D. students and visiting scholars from the Siglab at the University of Pennsylvania. They made my life delightful and fruitful.

ABSTRACT

Hybrid Eulerian-Lagrangian Topology Optimization

Yue Li

Advisor: Chenfanfu Jiang

Topology optimization generally considers a material redistribution and removal problem to satisfy prescribed design constraints while minimizing an objective function (e.g., structural compliance). Most traditional finite element based approaches are limited to the resolution of discretization with using supercomputers or a carefully designed and data structure and system dependent acceleration techniques. This thesis instead proposes a material point method inspired and based hybrid Eulerian-Lagrangian approach to address this problem. With this hybrid approach and the total decoupling from the design variables and simulation degree of freedoms, this proposed method can achieve considerably lower compliance given the same simulation time cost. We evaluate a comparison of the proposed method with the classic approach in topology optimization on extensive benchmark cases to demonstrate the effectiveness of our method.

Keywords: Topology Optimization, Material Point Method, Constrained Optimization, Structural Compliance.

TABLE OF CONTENTS

ACKNOWLEDGEMENT	ii
ABSTRACT	iii
LIST OF TABLES	vi
LIST OF ILLUSTRATIONS	ix
CHAPTER 1 : Introduction	1
CHAPTER 2 : Related Work	4
2.1 Topology Optimization	4
2.2 Physics-based Simulation	6
CHAPTER 3 : Problem Statement	7
3.1 General Objective in Topology Optimization	7
3.2 MPM Discretization	8
3.3 Linear Elasticity	10
CHAPTER 4 : Design Variable and Optimization Pipeline	11
4.1 Carrier Particles and Fixed Quadrature points	11
4.2 Objective Function and Constraint	12
4.3 Objective and Constraint Function Gradient	13
4.4 Stiffness Matrix Construction for Implicit MPM	13
4.5 Density Representation	14
4.6 Jacobian Matrix Construction	16
4.7 Boundary and Load Condition	16
4.8 Optimization Process	17

4.9	Other Choices of Design Variables	20
CHAPTER 5 :	Second Order Method	22
5.1	Motivation	22
5.2	Hessian Derivation	22
CHAPTER 6 :	Results, Comparisons, and Discussions	25
6.1	Results	25
6.2	Benchmark Comparisons	30
6.3	Ablation Study	32
CHAPTER 7 :	Conclusion and Outlook	37
APPENDIX		38
BIBLIOGRAPHY		60

LIST OF TABLES

TABLE 1 : Benchmark results and compliance values	59
---	----

LIST OF ILLUSTRATIONS

FIGURE 1 :	Illustration of quadrature particles, carrier particles, and Eulerian grid. Quadrature points are denoted with red dots, carrier particles are marked with blue dots, and the black grid is the MPM simulation grid. (a) refers to the initialization state and (b) could refer to any intermediate optimization state.	12
FIGURE 2 :	Initial state for the cantilever beam problem. Dirichlet boundary condition is set to the left most grid nodes illustrated by the red rectangle, and an external force load is added on the bottom right corner of the simulation domain.	18
FIGURE 3 :	Intermediate state after 60 iterations for the cantilever beam problem.	19
FIGURE 4 :	Converged result for the cantilever beam problem.	19
FIGURE 5 :	Failure case of optimize MPM particle position only. In this case, a downward external force is added on the bottom right grid corner of the design domain and fixing the left most grid nodes.	20
FIGURE 6 :	Failure case of optimize MPM particle position only with 1 million particles. In this case, a downward external force is added on the middle of the right most grid column of the design domain and fixing the left most grid nodes.	21
FIGURE 7 :	Exact Hessian and LBFGS comparison, the design domain is discretized by 20 x 10 simulation grid cells.	24
FIGURE 8 :	Exact Hessian and LBFGS comparison, the design domain is discretized by 80 x 40 simulation grid cells.	24

FIGURE 9 : Initial state for the Mitchell structure problem. This case is set to mimic the Mitchell structure Michell (1904). The design domain is discretized by 160 x 120 grid cells, a vertical force is added on the left denoted by the downward arrow. Red dots on the middle right of the right images show the position of Dirichlet boundary nodes. The movement and density changing of carrier particles are shown on the left of each figure.	25
FIGURE 10 : Intermediate state after 42 iteration for the Michell structure problem.	26
FIGURE 11 : Converged state after 150 iteration for the Michell structure problem. As it is depicted in this figure, the movement of carrier particles contributes greatly to form these cell like structures.	26
FIGURE 12 : Circle with multiple tangential loads. The square design domain is discretized by 200 x 200 grid cells.	27
FIGURE 13 : Bridge example. Left and right most grid nodal position is fixed. Force is added uniformly on the bottom most grid nodes. This design domain is discretized by 300 x 100 grid cells	27
FIGURE 14 : Plane shear example. Shear force is added uniformly on the top most grid nodes with bottom most nodes fixed. This design domain is discretized by 200 x 200 grid cells.	28
FIGURE 15 : Plane force example. Vertical force load is added onto the topmost grid nodes while left most grid nodes are fixed. This design domain is discretized by 200 x 100 grid cells.	28
FIGURE 16 : Low-resolution three-dimensional chair example. Force loads are demonstrated by the black arrow on the left image.	29

FIGURE 17 : Benchmark comparison with state-of-the-art SIMP method. Bar chart in the first row plots the compliance for both two methods. Second row plots the relative percentage that the proposed method is lower than SIMP.	31
FIGURE 18 : Compliance comparison grouped by volume. As demonstrated in this figure the proposed method show more advantage given less volume fraction constraint.	31
FIGURE 19 : Comparison with proposed method and remove step size constraint on x_p and ρ_p at third iteration. Left most is proposed method with step size constraint on both x_p and ρ_p , middle image is remove step size constraint on x_p , right most image is remove step size constraint on ρ_p	32
FIGURE 20 : Comparison with proposed method and remove step size constraint on x_p and ρ_p at 40th iteration.	33
FIGURE 21 : Comparison with proposed method and remove step size constraint on x_p and ρ_p at final state.	33
FIGURE 22 : Objective energy plot of proposed method and remove step size constraint on either x_p or ρ_p . Note that at first couple of iterations those do not have constraint on step size experienced large energy variation, resulting in higher compliance local minima.	34
FIGURE 23 : Volume plot of proposed method and remove step size constraint on either x_p or ρ_p . Without constraint on step size volume constraint satisfaction is also unstable.	34
FIGURE 24 : Gradient infinity norm plot of proposed method and remove step size constraint on either x_p or ρ_p	35

CHAPTER 1 : Introduction

Topology Optimization aims to find the optimal material distribution of a prescribed design domain given certain loads and boundary conditions. It has been widely accepted and adopted by different types of industries (e.g.car manufacturing, acoustics, aeronautics, architectural design), and a range of fields. (e.g.mathematics, physics, computer science). Recently, emerging mutual interests from computer graphics and topology optimization communities have manifested. For instance, the Deformable Simplicial Complex method is used to introduce holes in Misztal and Bærentzen (2012). Reciprocally, the introduction of carrier particles in this proposed method comes directly from the hybrid idea of Lagrangian particles and an Eulerian grid in the material point method (MPM). It is fascinating to see the future possibilities of the crossing of these two fields.

As it is shown in bones, bird beaks, and many other intricate structures by mother nature, it is generally assumed that with more detailed geometry features, the topological structural compliance is lower. Previous work has supported this idea by either using supercomputers Aage et al. (2017) or using a single computer with a carefully designed data structure Liu et al. (2018) to solve the topology optimization problem at super high resolution. Traditionally, the topology optimization problem is often explored with finite element methods, and the optimal material distribution is acquired with relocating and removal of the design variable. Both these two methods employ FEM to solve for nodal displacement on each element. It is worth noticing that in their approach, even though each two-dimensional quadrangle element has four nodal simulation degree of freedoms (DoFs), they share one volume. In order to account for a higher number of DoFs on optimization variables, they have to increase the DoFs on simulation variables as well. The time cost is expensive even with 8000 cores or a narrow-band block-based FEM. Another problem with FEM method happens when solid cracks Belytschko et al. (1996) or large deformation manifested. It could be rather time consuming to perform remeshing and there isn't a universal remeshing strategy yet. To this end, this thesis proposes a hybrid method that is able to capture more

detailed geometry features with more DoFs per cell while maintaining the same simulation cost. Consequently, this method achieves lower structural compliance value compared to the state-of-the-art methods.

Lower structural compliance, even less than one percent, is an excellent contribution to both manufacturing and research communities. If converting the weight savings into a reduction in fuel cost, the amount is rather significant Aage et al. (2017). However, as it is pointed out in Maute and Sigmund (2013), albeit a large variety of methods has been explored, they are either not providing substantial novel contributions or lacking comparison with benchmark experiments. It seems hard to identify the practical value if every method is evaluated individually, or even worse, not evaluated at all. With these sharp comments in mind, this thesis presents a novel approach in addressing the topology optimization problem, meanwhile, comparing this method to the current state-of-the-art methods on a benchmark consists of various load, boundary conditions as well as different volume fraction constraint.

As it is aforementioned, in order to address the problem from a different point of view, this thesis draws ideas specifically from the material point method, which combines an Eulerian grid and Lagrangian particles. It is more natural for the MPM community that each particle or quadrature point has its own attribute. Instead of increasing the number of finite elements, which add significantly more cost in solving linear systems of equations for simulation DoFs. The proposed method allows more DoFs by enabling multiple volumes inside a simulation grid cell. However, since these MPM particles serve as quadrature points, naively choosing them to be optimization variables will cause significant numerical errors. By moving these points, it is essentially putting quadrature points at arbitrary positions. To take advantage of MPM while keeping the numerical accuracy. This thesis uses a similar method to decouple design variables from integration quadrature points from an emerging topology optimization method, moving morphable components (MMC) Guo et al. (2014). To the best knowledge of this thesis, it is the first time that the material point method is utilized in addressing topology optimization problems.

The contribution of this thesis could be summarized as:

- A hybrid Eulerian-Lagrangian method achieving lower structural compliance than the state-of-the-art FEM method at the same simulation cost.
- To the best knowledge of the author, the proposed method is the first material point method minimizing structural compliance in topology optimization.
- Benchmark comparisons with state-of-the-art methods on various loads, boundary configuration, and volume constraints.
- Exploring second-order optimization method in topology optimization.

This thesis is organized as the following. Chapter 2 gives an overview of the most related work of the proposed method. Chapter 3 presents the problem statement of the general topology optimization problem and the objective function with the proposed method. The choice of design variables, optimization pipeline, and key component derivation is demonstrated in Chapter 4. Hessian derivation and comparisons with L-BFGS are listed in Chapter 5. The results of the proposed method on various design cases are shown and benchmark comparisons and evaluations are provided in chapter 6. Chapter 6 also contains an ablation study on the particular choices made in this thesis. Lastly, chapter 7 concludes the thesis and discusses future research directions.

CHAPTER 2 : Related Work

2.1. Topology Optimization

Topology Optimization refers to the method of finding an optimal material distribution of a design domain given certain loads and boundary conditions. The final density distribution should only consist of binary values, where 0 denotes a void region, and 1 indicates solid material. Since the homogenization method was proposed by Bendsøe and Kikuchi (1988) as the first topology optimization method, different research communities have chosen different design variables to represent the problem. Some choose to work on density-based approaches Bendsøe (1989); Mlejnek (1992) while others use different variables to explicitly or implicitly relate to density such as level set Wang et al. (2003); Allaire et al. (2004). The design domain is generally discretized by a large number of finite elements to compute the structural response. Optimal Criteria (OC) and Method of Moving Asymptotes (MMA) Svanberg (1987) is mostly used for optimization. Topology optimization is a well-established research area and is gaining increasing attention from a wide range of fields. It is beyond the scope and ability of this thesis to conduct a conclusive survey. Therefore, only the works that closely influence the development of the method described by this thesis is discussed here. Please refer to Maute and Sigmund (2013) for a much more detailed review of related work.

Density Based Approach

Solid Isotropic Material with Penalization Method (SIMP) Sigmund (2001) is one of the most popular methods used to address this optimization problem due to its conceptual and computational simplicity. The binary requirement on the design variable is relaxed, and intermediate density is allowed. SIMP employs a power-law method as penalization to reduce such intermediate states. The relation between material attributes and the density of the material is given by power-law. Essentially, the material attribute $E(\rho)$ is replaced by $\rho^p E_0$ where E_0 is Young's modulus of solid material. p is usually set to 3 to reduce the grey area while ensuring not rapidly converging to local minima. Note that when p is

equal to 1, the problem is convex. Studies have been applied in solving the convex problem first to acquire a global solution, then gradually increase the power to reduce intermediate values and search for local minima that are not far away from the global minima known as *Continuation Method*. SIMP approach is widely utilized due to its mesh independence nature, namely, the number of iteration required to solve the problem does not vary with the subdivision of the finite element mesh. By locally adding and removing material to satisfy the volume fracture constraint with the penalization of intermediate density, numerical instabilities (mostly known as checkerboard patterns) may occur in this method. Structures with checkerboard patterns are known to have lower structural compliance value, thus, additional measures must be incorporated to circumvent this kind of local minima. Usually, different kinds filters (Wang et al. (2011); Sigmund and Maute (2012); Sigmund (2007)) on the gradient of the compliance are utilized.

Level Set Based Approach

Level set methods define the boundary of void and solid region to represent a given geometry. Everything inside the level set is considered to be solid. Unlike density-based approaches with heuristic, since the evolution of the geometry only happen at the boundary where the derivative is non-zero, adding holes into the prescribed domain is not automatically handled. Separate steps are necessary for new holes generation, which may result in worse convergence behavior Maute and Sigmund (2013). Note that intermediate density may still exist near the boundary. One particular flavor of level set based methods, Moving Morphable Components (MMC), facilitates the research direction of this thesis. The idea of MMC is firstly introduced by Guo et al. (2014). MMC methods use low dimension morphable components, superellipse level set, that has the capability of moving, deforming, and overlapping, to address the same problem. It is worth noting that level sets are not necessary for the geometry description, and pure Lagrangian description is applicable as well Zhang et al. (2016). This method aims to substantially reduce the number of design variables to solve large scale problems. By greatly reducing the number of design variables, this method is limited by the fact that they are pursuing local minima in a much lower dimension. To

acquire a solution with rich geometry features, a larger number of design variables have to be utilized as well. The idea that this method proposed, separating the design variable with optimization variables enlighten the development of this thesis.

2.2. Physics-based Simulation

Material Point Method (MPM)

MPM Sulsky et al. (1995) is a hybrid Lagrangian-Eulerian method widely used in different fields of research(e.g. computer graphics, civil engineering, mechanical engineering, etc.). With the capability of handling large deformation and different material coupling, MPM has been considered as a top choice in physics-based simulation (e.g. fracture Wolper et al. (2019), viscoelastic and elastoplastic solids Fang et al. (2019), snow Stomakhin et al. (2013), sand Klár et al. (2016) and mixtures Tampubolon et al. (2017)). Lagrangian particles, material points, are used to track quantities like mass, momentum, and deformation gradient while a regular Eulerian grid is built at each iteration step to evaluate force and update velocity. Particle quantity is then updated from the interpolation of nodal quantities. MPM is considered to be a meshfree method since the temporary grid is built and discarded after each simulation step. For more details regarding MPM, please refer to Jiang et al. (2016). Both density-based or level set-based topology optimization approach suffered from the jagged edges with finite elements, albeit plotting zero-level contour disguises such effect Maute and Sigmund (2013). Lagrangian particles could form more detailed shapes to reduce jagged edges. However, topology change is not differentiable with a purely Lagrangian method. Given this conflicting situation, this thesis aims to take the advantages of the hybrid Lagrangian-Eulerian nature of MPM to form a more detailed structure achieving lower compliance.

CHAPTER 3 : Problem Statement

3.1. General Objective in Topology Optimization

This thesis intends to address the topology optimization problem by minimizing the compliance value $c(x)$.

$$\min_x C(x) = H(U(x), x) \quad (3.1)$$

subject to

$$\begin{cases} f(U(x), x) = F \\ V(x) - V_0 \leq 0 \\ \rho(x) = 0 \quad \text{or} \quad 1 \end{cases} \quad (3.2)$$

where F, U, f, V_0, ρ is external force load, nodal displacement, internal force, initial volume fraction and material density respectively.

$f(U(x), x)$ could be either a linear or non-linear equilibrium state that the system should satisfy. This thesis only concerns linear elasticity and in order to use gradient based method continuous density variable is considered. With this specification the general problem could be written as

$$\min_x C(x) = F^T U(x) \quad (3.3)$$

subject to

$$\begin{cases} K(x)U(x) = F \\ V(x) - V_0 \leq 0 \\ 0 \leq \rho(x) \leq 1 \end{cases} \quad (3.4)$$

where K is the stiffness matrix.

3.2. MPM Discretization

Denote structural compliance as linear elastic potential reads

$$e(x) = \int_{\Omega_0} \Psi(F) dX \quad (3.5)$$

where Ω_0 is the material space the elastic body lies in and Ψ is the elastic energy density function. F is the the deformation gradient.

$$F = \frac{\partial \phi}{\partial X} \quad (3.6)$$

where ϕ is the mapping function from material space to deformed space and X is the material space position, such that

$$x = \phi(X, t) \quad (3.7)$$

where x is the deformed position and t denote time step. For hyperelastic materials where the first Piola Kirchoff stress is related to an elastic potential energy density Ψ by

$$P = \frac{\partial \Psi}{\partial F} \quad (3.8)$$

To discretize this compliance on the Eulerian grid using Lagrangian variables with the material point method. The compliance is defined as total elastic potential of all Lagrangian particles. If we refer to the vector of all grid nodes x_i as \hat{x}_I , then the MPM approximation to the total elastic potential can be written as

$$e(x) = \int_{\Omega_0} \Psi(F) dX \approx \sum_p V_p \Psi_p(F_p(\hat{x}_I)) \quad (3.9)$$

The structural compliance then becomes

$$C(x) = \sum_p Vp\Psi_p(F_p(\hat{x}_I)) \quad (3.10)$$

subject to

$$f_I(\hat{x}_I) = b \quad (3.11)$$

where f_I is elastic force on Eulerian grid nodes and b is external force added. \hat{x}_I is the nodal position after at equilibrium state. Vp, Ψ_p, F, x_p are the volume, energy density, deformation gradient and position of particle p respectively.

Apply Taylor expansion on $f_I(\hat{x}_I)$ at initial grid state x_I and truncate at first order we have

$$f_I(\hat{x}_I) = f_I(x_I) - \nabla_{x_I}^2 \Psi_P(I)(\hat{x}_I - x_I) \quad (3.12)$$

Since $f_I(x_I)$ at rest state is zero. The constraint becomes

$$-\nabla_{x_I}^2 \Psi_P(I)(\hat{x}_I - x_I) + b_I = 0 \quad (3.13)$$

Apply Taylor expansion on Ψ_P at x_I

$$\Psi_P = \Psi_P(x_I) + \nabla_{x_I} \Psi_P(I)(\hat{x}_I - x_I) + \frac{1}{2}(\hat{x}_I - x_I)^T \nabla_{x_I}^2 \Psi_P(I)(\hat{x}_I - x_I) \quad (3.14)$$

since $\Psi_P(x_I)$ and $\nabla_{x_I} \Psi_P(I)$ are zero, our Ψ_P becomes just $\frac{1}{2}(\hat{x}_I - x_I)^T \nabla_{x_I}^2 \Psi_P(I)(\hat{x}_I - x_I)$

denote $\nabla_{x_I}^2 \Psi_P(I)$ as K and $(\hat{x}_I - x_I)$ as u , our problem is given by

$$\min_x = \frac{1}{2} u(x)^T K(x) u(x) \quad (3.15)$$

subject to

$$K(x)u(x) = b \quad (3.16)$$

The gradient of the objective energy is given by

$$\frac{\partial \frac{1}{2}u(x)^T K(x) u(x)}{\partial x} = u(x)^T K(x) \frac{\partial u}{\partial x}(x) + \frac{1}{2} u(x)^T \frac{\partial K}{\partial x}(x) u(x) \quad (3.17)$$

Differentiating both side of equation 3.16 gives

$$\frac{\partial K}{\partial x}(x) u(x) + K(x) \frac{\partial u}{\partial x}(x) = 0 \quad (3.18)$$

substitutes $K(x) \frac{\partial u}{\partial x}(x)$ in equation 3.18 the gradient becomes

$$\frac{\partial \frac{1}{2}u(x)^T K(x) u(x)}{\partial x} = -\frac{1}{2} u(x)^T \frac{\partial K}{\partial x}(x) u(x) \quad (3.19)$$

3.3. Linear Elasticity

Only linear elasticity is considered in this thesis due to its simplicity in practice. With linear elasticity, the final converged state does not vary from different scaling of the force load. The linear elasticity energy density function Ψ is defined as a function of particle deformation gradient F as

$$\Psi(F) = \mu \epsilon : \epsilon + \frac{\lambda}{2} \text{tr}^2(\epsilon) \quad (3.20)$$

where ϵ is the small strain tensor given by

$$\epsilon = \frac{1}{2}(F + F^T) - I \quad (3.21)$$

and μ, λ are Lamé parameters related to Young's modulus E and Poisson's ratio ν . The relation is given by

$$\mu = \frac{E}{2(1+\nu)}, \quad \lambda = \frac{E\nu}{(1+\nu)(1-2\nu)} \quad (3.22)$$

The first Piola Kirchoff stress for linear elasticity is then

$$P = \mu(F + F^T - 2I) + \lambda \text{tr}(F - I)I \quad (3.23)$$

CHAPTER 4 : Design Variable and Optimization Pipeline

4.1. Carrier Particles and Fixed Quadrature points

Since particles serve as quadrature in MPM, arbitrary movement of these particles may cause large numerical errors(Section 4.8). Besides, computing $\frac{\partial K}{\partial x}$ is more complicated when quadrature is considered as a design variable. To separate design variables from quadrature points, carrier particles are introduced. Carrier particle is defined in the entire design domain with the free capability to move and changing its density. With this separation, design variables are totally decoupled from simulation DoFs. Given simulation domain discretized via Eulerian grid, fixed number particles Q are placed inside each grid cell at fixed locations serving as quadrature points. The density of these particles are computed as the weighted sum of neighboring carrier particles C using equation 4.12. An illustration is shown in Fig. 1. With this transfer scheme, multiple DoFs on material density is allowed inside one cell, depending on the number of quadrature points. To add more DoFs on material density, increasing the simulation DoFs is usually considered in FEM based topology optimization researches. Nonetheless, this is impractical when the optimization is already evaluated on a high-resolution discretization. Thanks to this consideration, the proposed method is able to manifest the sub-cell structure and reduced the jagged edges problem with a single density per cell to a great degree.

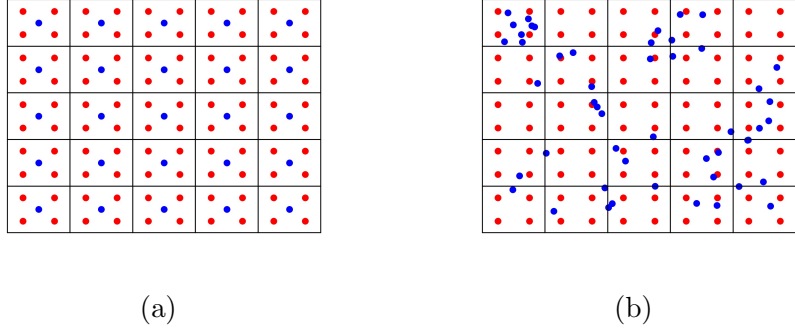


Figure 1: Illustration of quadrature particles, carrier particles, and Eulerian grid. Quadrature points are denoted with red dots, carrier particles are marked with blue dots, and the black grid is the MPM simulation grid. (a) refers to the initialization state and (b) could refer to any intermediate optimization state.

4.2. Objective Function and Constraint

With x_p , ρ_p defined to be the position and density of carrier particles. The objective function in equation 3.15 becomes

$$\min_{x_p, \rho_p} = \frac{1}{2} u(\rho_p(x_p))^T K(\rho_p(x_p)) u(\rho_p(x_p)) \quad (4.1)$$

subject to

$$\begin{cases} Ku = f \\ \frac{\sum_i \rho_{qp_i}}{\sum_i 1} \leq \tilde{V} \end{cases} \quad (4.2)$$

where ρ_{qp} is the density of the fixed quadrature points, and \tilde{V} is the target volume fraction.

$$\rho_{qp} = \sum_i \rho_{01}, \quad (4.3)$$

where ρ_{01} is the density after a wrapper function. The wrapper function is given by equation 4.15. This wrapper function is crucial in this method. Since the gathering of particles can form harder material and yet satisfy volume constraint.

4.3. Objective and Constraint Function Gradient

Denote objective function as L , the Jacobian of the objective function is given by

$$\frac{\partial L}{\partial x} = -\frac{1}{2} u^T \sum_i \frac{\partial K}{\partial \rho_{qp_i}} \frac{\partial \rho_{qp_i}}{\partial x} u \quad (4.4)$$

Denote the constraint function as g , the Jacobian of the constraint function is then,

$$\frac{\partial g}{\partial x} = \sum_i \frac{\partial \rho_{qp_i}}{\partial x} \quad (4.5)$$

This thesis also assumes the material attribute, Young's modulus, of each particle scales linearly with its density.

$$E_p = \rho_p E_0 \quad (4.6)$$

where E_0 is Young's modulus for solid material.

4.4. Stiffness Matrix Construction for Implicit MPM

Following eqn. 3.10 the spatial discretization of the stress-based forces with MPM is given as

$$-f_i(\hat{x}) = \frac{\partial e}{\partial \hat{x}_i}(\hat{x}) = \sum_p V_p \frac{\partial \Psi}{\partial F}(\hat{F}_p(\hat{x})) F_p^T \nabla \omega_{iq} \quad (4.7)$$

where ω_{iq} is the interpolation function between grid node i and particle q . In this thesis, quadratic B spline is used as kernel function and the dyadic products of one-dimensional interpolation functions is used as the grid basis functions where $\omega_{iq} = N(x_q)$ and

$$N(x_q) = N\left(\frac{1}{h}(x_q - x_i)\right) N\left(\frac{1}{h}(y_q - y_i)\right) N\left(\frac{1}{h}(z_q - z_i)\right) \quad (4.8)$$

For the three dimensional case, quadratic B spline kernel is given by

$$N(x) = \begin{cases} \frac{3}{4} - |x|^2, & 0 \leq R < \frac{1}{2} \\ \frac{1}{2}(\frac{3}{2} - |x|)^2, & \frac{1}{2} \leq R < \frac{3}{2} \\ 0, & \frac{3}{2} \leq x \end{cases} \quad (4.9)$$

The stiffness matrix K is therefore computed as

$$K = \frac{\partial^2 e}{\partial x_i \partial x_j} = -\frac{f_i(\hat{x})}{\partial x_j} = \sum_i \sum_p [V_p \rho_p \frac{\partial^2 \Psi(F_p)}{\partial F_p \partial F_p} : (\sum_j (\nabla \omega_{jp})^T F_p^0)] \quad (4.10)$$

where p is the index for all particles in the range of the kernel function of node i , V_p^0 , F_p^0 , $\Psi(F_p)$ are the volume, deformation gradient at initial state and energy density of particle p respectively. The notation $C = A : B$ denotes $C_{ij} = A_{ijkl}B_{kl}$ with summation implied on indices kl .

To write out K with index notation

$$K_{id+\alpha, jd+\beta} = V_p (F_p^{0T} \nabla \omega_{ip})_\delta \rho_p \frac{\partial^2 \Psi(F_p)}{\partial F_{p,\alpha\delta} \partial F_{p,\beta\omega}} (F_p^{0T} \nabla \omega_{jp})_\omega \quad (4.11)$$

4.5. Density Representation

In this thesis, the density of each quadrature particle is computed as the weighted sum of its neighboring carrier particles using a spherical kernel.

$$\rho_{SPH_i} = \sum_j \rho_{c_j} V_{c_j} W(R) \quad (4.12)$$

where $W(R)$ is a kernel function. R is the normalized distance between particle p_i and

particle p_j . In this thesis, this kernel function with cubic spline is given by

$$W(R) = \frac{15}{7\pi h^2} \begin{cases} \frac{R^3}{2} - R^2 + \frac{2}{3}, & 0 < R < 1 \\ \frac{(2-R)^3}{2}, & 1 < R < 2 \\ 0, & otherwise \end{cases} \quad (4.13)$$

$$dW(R) = \frac{15}{7\pi h^2} \begin{cases} \frac{3}{2}R^2 - 2R, & 0 < R < 1 \\ \frac{-(2-R)^2}{2}, & 1 < R < 2 \\ 0, & otherwise \end{cases} \quad (4.14)$$

where h is the normalization factor. To prevent the summed density from becoming larger than one, a wrapper function is further added on top of ρ_p .

The wrapper function considered in this thesis is defined as follows.

$$\rho_{01}(\rho) = \begin{cases} \rho, & 0 \leq \rho < 1 - \epsilon \\ \frac{(\rho+\epsilon-1)^2}{4\epsilon} + \rho, & 1 - \epsilon \leq \rho < 1 + \epsilon \\ 1, & otherwise \end{cases} \quad (4.15)$$

The wrapper function is designed such that it is linear function of ρ until it almost reach its upper bound. If ρ is larger than ρ_{max} its value will be 1 and the derivative will be zero to prevent particle aggregation. Note that at exact ρ_{max} this function has C_1 continuity.

Following SIMP, to ensure the existence of a solution, the penalization of the density is also performed to remove intermediate density between 0 to 1. The final density at each quadrature i then

$$\rho_{qp_i} = (\rho_{01})^p \quad (4.16)$$

with p is the penalty power, it is chosen to be 3 in this thesis.

4.6. Jacobian Matrix Construction

Differentiating K with respect to x gives

$$\frac{\partial K}{\partial x} = \sum_i \frac{\partial K}{\partial \rho_{qp_i}(x)} \frac{\partial \rho_{qp_i}(x)}{\partial x} \quad (4.17)$$

For linear elasticity $\frac{\partial^2 \Psi(F_p)}{\partial F_p \partial F_p}$ is constant and the objective formulation is further simplified given that the deformation gradient at initial state is always identity.

$$\frac{\partial K_{id+\alpha,jd+\beta}}{\partial \rho_{qp_i}(x)} = V_q(\nabla \omega_{iq})_\delta \frac{\partial^2 \Psi(F_q)}{\partial F_{q,\alpha\delta} \partial F_{q,\beta\omega}} (\nabla \omega_{jq})_\omega \quad (4.18)$$

$$\frac{\partial \rho_{qp_i}}{\partial x} = \frac{\partial \rho_{qp_i}}{\partial \rho_{01}} \frac{\partial \rho_{01}}{\partial \rho_{SPH_i}} \frac{\partial \rho_{SPH_i}}{\partial x} \quad (4.19)$$

$$\frac{\partial \rho_{SPH_i}}{\partial x_{c_j}} = V_{c_j} W(R) \quad (4.20)$$

$$\frac{\partial \rho_{SPH_i}}{\partial x_{c_j}} = \rho_{c_j} V_{c_j} \frac{dW(R)}{dR} \frac{\partial R}{\partial x_{c_j}} \quad (4.21)$$

4.7. Boundary and Load Condition

The boundary condition is added to MPM grid nodes. Forces are added on to certain quadratures and then transferred into the grid node in their kernel radius.

$$b_i = \sum_q F_q \omega_{iq} \quad (4.22)$$

4.8. Optimization Process

4.8.1. Optimization Pipeline

The optimization pipeline for x_p and ρ_p is given by Algorithm 1.

Algorithm 1 Optimize Carrier Particles Position and Density

```

Initialization initialize particles position  $x_p$ , density  $\rho_p$  external force  $f$ , boundary condition  $\tau$ ,  $x_{min}$ ,  $x_{max}$ ,  $\rho_{min}$ ,  $\rho_{max}$ 
while not converge do
    build  $K$  with  $x_p^i$  and  $\rho_p^i$ 
     $u \leftarrow \text{solve } Ku = f$ 
     $L \leftarrow \frac{1}{2}u^T Ku$ 
     $\frac{\partial L}{\partial x_p, \rho_p} \leftarrow \frac{1}{2}u^T \frac{\partial K}{\partial x_p, \rho_p} u$ 
     $x_p^{i+1}, \rho_p^{i+1} \leftarrow \text{mmasub}\left(\frac{\partial L}{\partial x_p, \rho_p}, x_{min}, x_{max}, \rho_{min}, \rho_{max}\right)$ 
end while

```

mmasub is employing the method of moving asymptotes to update the optimization variable. It has been proven in practice to address the ill-scaled gradient issue better. In order to help stabilize the algorithm, box constraint is added to x_{min} and x_{max} at each iteration to regularize position movement at each iteration. In the implementation of this thesis, this constraint is set to be ten times simulation grid spacing. In order to not let density dominant the optimization process, density changing per iteration is set to be 0.5. There is no absolute upper and lower bound for the position of these particles and no upper bound for density. Minimal density is set to zero. The importance of adding this step size constraint is further discussed in section 6.3.

4.8.2. Optimization Step Illustration

An optimization process is demonstrated on the standard cantilever beam problem. The initial carrier particles are uniformly sampled in the design domain with the same density value such that the equality volume constraint is satisfied at the initial state(Fig. 2). From Fig. 2 to Fig. 4. The top image denotes density value at all quadrature points mapping 0 to 1 density to blue to red. The bottom image visualizes the density and position of carrier particles. For this example, the design domain is discretized by 120 x 40 simulation cells. Each cell contains four uniformly distributed quadrature points. The kernel size for

all quadrature points is set to be 1.25 times simulation grid spacing. The upper bound of the target volume fraction is $0.4 V_0$. A vertical force is added on the bottom right corner of the simulation domain.



Figure 2: Initial state for the cantilever beam problem. Dirichlet boundary condition is set to the left most grid nodes illustrated by the red rectangle, and an external force load is added on the bottom right corner of the simulation domain.

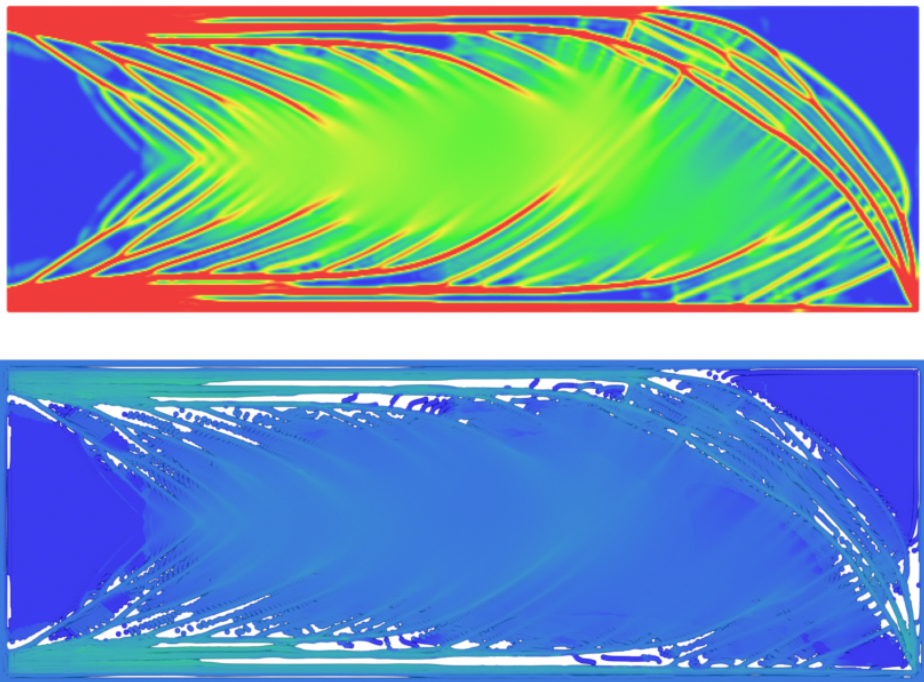


Figure 3: Intermediate state after 60 iterations for the cantilever beam problem.

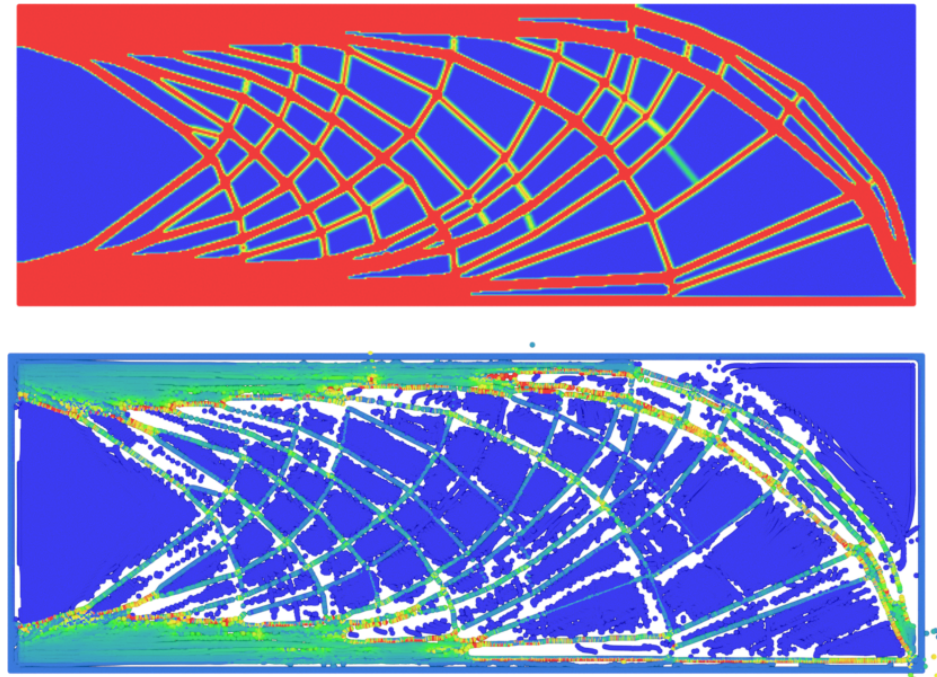


Figure 4: Converged result for the cantilever beam problem.

4.9. Other Choices of Design Variables

With a basic idea of the material point method, it might occur to one that either the position or both density and position of the Lagrangian particles could be chosen as design variables. If solely density of each particle is considered, it should be almost identical to SIMP hence losing the benefits of using Langrangian particles per se. With the development of this thesis, both optimizing particle position or simultaneously optimize with density have been implemented and tested. Since they are not chosen as the final method, only results and drawbacks are discussed here. For more detailed information, the reader is more than welcome to contact the author for discussions. For the case where only the position is considered to be an optimization variable, the detailed geometric feature does exist, particularly in high-resolution scenarios. Fig. 6. However, a large number of particles get trapped inside cell-like structures, leading to non-converging behavior. The optimization also considers a box constraint for all particles.

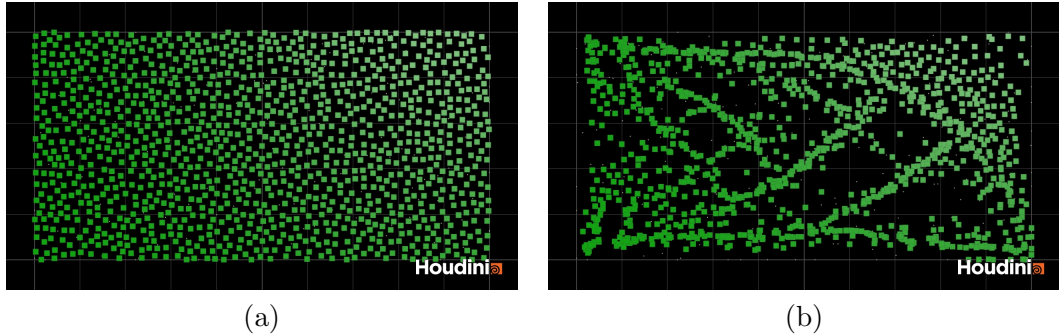


Figure 5: Failure case of optimize MPM particle position only. In this case, a downward external force is added on the bottom right grid corner of the design domain and fixing the left most grid nodes.

When considering density as an extra optimization variable, it seems like those trapped particles or those that are trying to escape the box constraint of the simulation domain could change to lower the objective function. It turned out to be not the case due to the fundamental problem of this method aforementioned in Section 4.1. As a mesh free method, the quadrature points should remain regularly spaced. However, due to the nature of this problem, the movement of particles are very likely to form irregular shapes which will lower

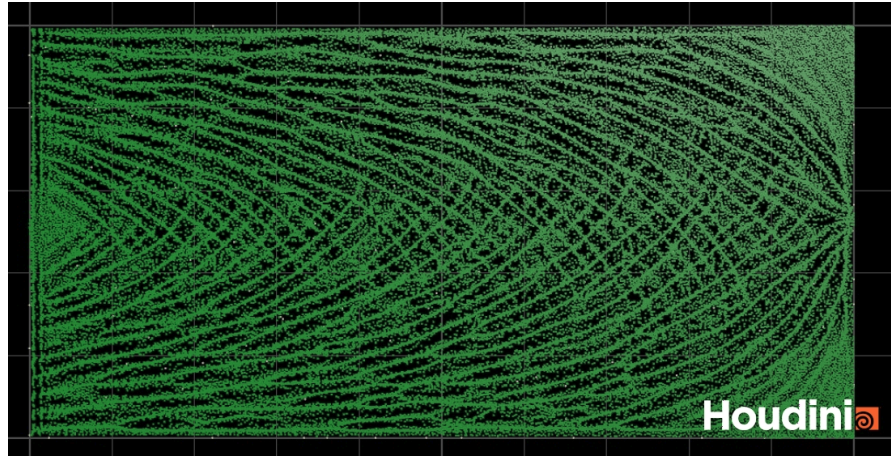


Figure 6: Failure case of optimize MPM particle position only with 1 million particles. In this case, a downward external force is added on the middle of the right most grid column of the design domain and fixing the left most grid nodes.

the accuracy of the mesh free method. With this method, it is also hard to explicitly define the volume fraction constraint.

CHAPTER 5 : Second Order Method

5.1. Motivation

Although the parameters for MMA are fixed for all experiments presented in this thesis, the author is aware that changing these parameters could lead to different structural compliance values. Tuning these values is not the concern of this thesis; however, it is of the interest of this thesis to see whether, with second-order information, there could be no need finding optimal parameters. Besides, even with regularization on the step size of optimization variables, the convergence speed is still relatively slow compared to SIMP. With MMA, both the derivative of x_p and ρ_p is passed, it is hard to decide whether the scale of these two gradients causes the slow convergence of the optimizer. It would be interesting to see whether scale the gradient with the Hessian matrix will speed up the convergence.

5.2. Hessian Derivation

Following equation 3.19, one can further compute the Hessian of the objective function.

$$\frac{\partial^2(\frac{1}{2}u(x)^T K(x)u(x))}{\partial x^2} = u(x)^T \frac{\partial K}{\partial x}(x) K^{-1} \frac{\partial K}{\partial x}(x) u(x) - \frac{1}{2} u(x)^T \frac{\partial^2 K}{\partial x^2}(x) u(x) \quad (5.1)$$

Derivation of $\frac{\partial^2 K}{\partial x^2}$ is computed as.

$$\frac{\partial^2 K}{\partial x^2} = \sum_i \left(\frac{\partial^2 K}{\partial \rho_{qp_i}^2} \frac{\partial \rho_{qp_i}}{\partial x} + \frac{\partial K}{\partial \rho_{qp_i}} \frac{\partial^2 \rho_{qp_i}}{\partial x^2} \right) \quad (5.2)$$

where $\frac{\partial^2 K}{\partial \rho_{qp_i}^2}$ is zero.

$$\frac{\partial \rho_{qp_i}^2}{\partial x^2} = \frac{\partial^2 \rho_{qp_i}}{\partial \rho_{01}^2} \frac{\partial \rho_{01}}{\partial x} + \frac{\partial \rho_{qp_i}}{\partial \rho_{01}} \frac{\partial^2 \rho_{01}}{\partial x^2} \quad (5.3)$$

The bottleneck of this method is due to the existence of K^{-1} . To compute $K^{-1} \frac{\partial K}{\partial x}(x) u(x)$

is essentially to solve a number of linear systems. The linear systems are given by

$$Ka = \left(\frac{\partial K}{\partial x}(x)u(x) \right)_b \quad (5.4)$$

where a is the a column vector at b th column in matrix $K^{-1} \frac{\partial K}{\partial x}(x)u(x)$.

In the implementation of this thesis, K is pre-factorized and then used in solving the above linear systems in parallel. The number of linear systems solving required is the number of carrier particles. In Fig. 7 and 8, comparison of using exact Hessian and quasi-Newton method, L-BFGS, is made. As can be seen from these two figures, the objective minimization process is much smoother with the exact Hessian being used. Since MMA does not utilize the Hessian matrix in its optimization process, IPOPT Wächter and Biegler (2006) library is used for this task. With IPOPT a Lagrangian function is defined as

$$L = f(x) + g(x)^T \lambda \quad (5.5)$$

where $f(x)$ is the objective function, $g(x)$ is a set of constraint functions and λ are the Lagrangian multipliers. With the constraint on volume fraction, the final Hessian of the Lagrangian for this problem is given by

$$\nabla^2 L = \sigma_f \nabla^2 f(x) + \sum_{i=1}^m \lambda_i \nabla^2 g_i(x) \quad (5.6)$$

where $m = 1$. For the following experiments, the initial μ for barrier function is set to 1e-8 using monotone strategy.

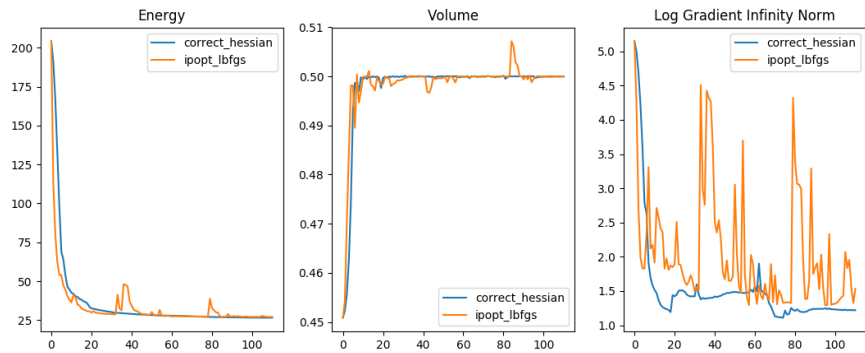


Figure 7: Exact Hessian and LBFGS comparison, the design domain is discretized by 20×10 simulation grid cells.

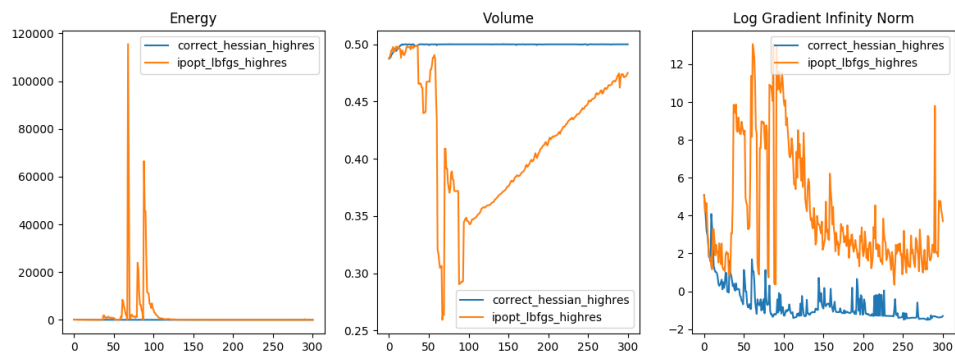


Figure 8: Exact Hessian and LBFGS comparison, the design domain is discretized by 80×40 simulation grid cells.

CHAPTER 6 : Results, Comparisons, and Discussions

6.1. Results

Different cases with various boundary and load conditions are shown in this section. Both carrier particle information and the density distribution on quadrature points are visualized. Noticing that adding carrier position as optimization variables allows detailed geometry features to manifest even at a relatively low-resolution simulation grid. For simplicity, only the iteration process of the first example is shown.

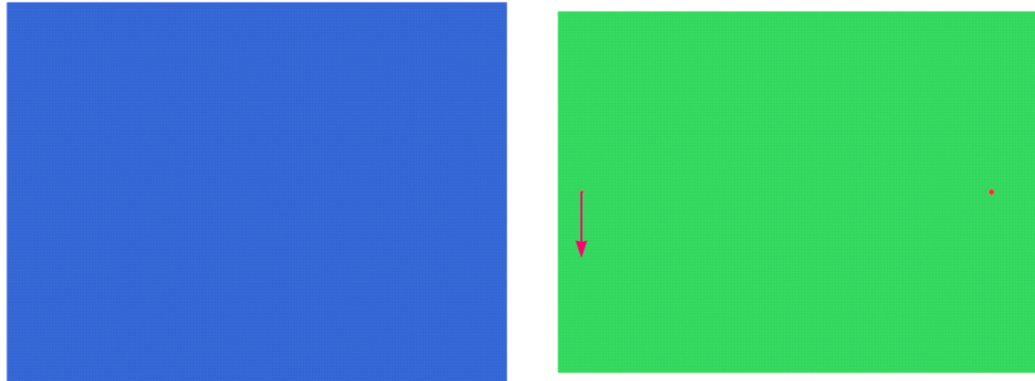


Figure 9: Initial state for the Mitchell structure problem. This case is set to mimic the Mitchell structure Michell (1904). The design domain is discretized by 160 x 120 grid cells, a vertical force is added on the left denoted by the downward arrow. Red dots on the middle right of the right images show the position of Dirichlet boundary nodes. The movement and density changing of carrier particles are shown on the left of each figure.

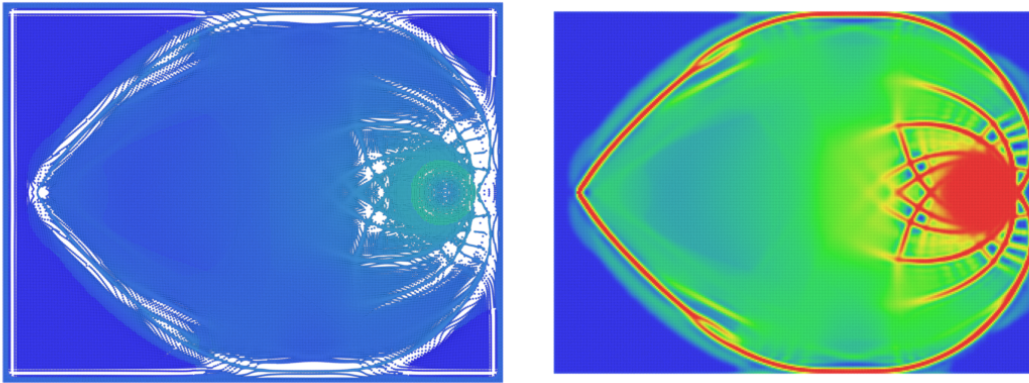


Figure 10: Intermediate state after 42 iteration for the Michell structure problem.

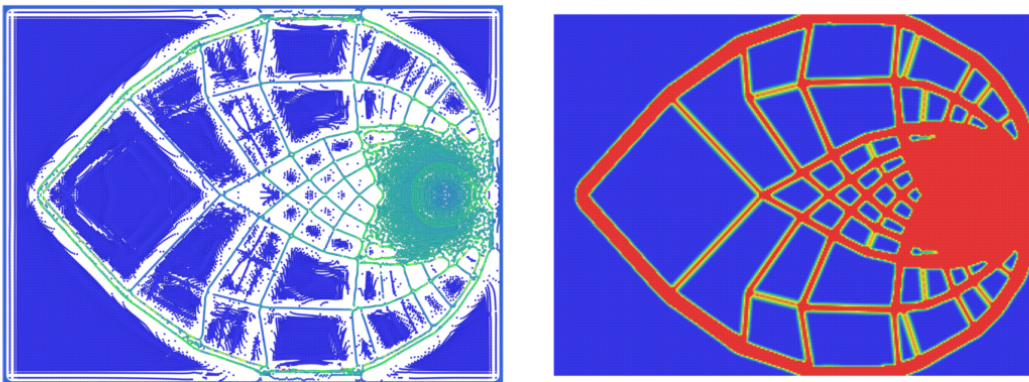


Figure 11: Converged state after 150 iteration for the Michell structure problem. As it is depicted in this figure, the movement of carrier particles contributes greatly to form these cell like structures.

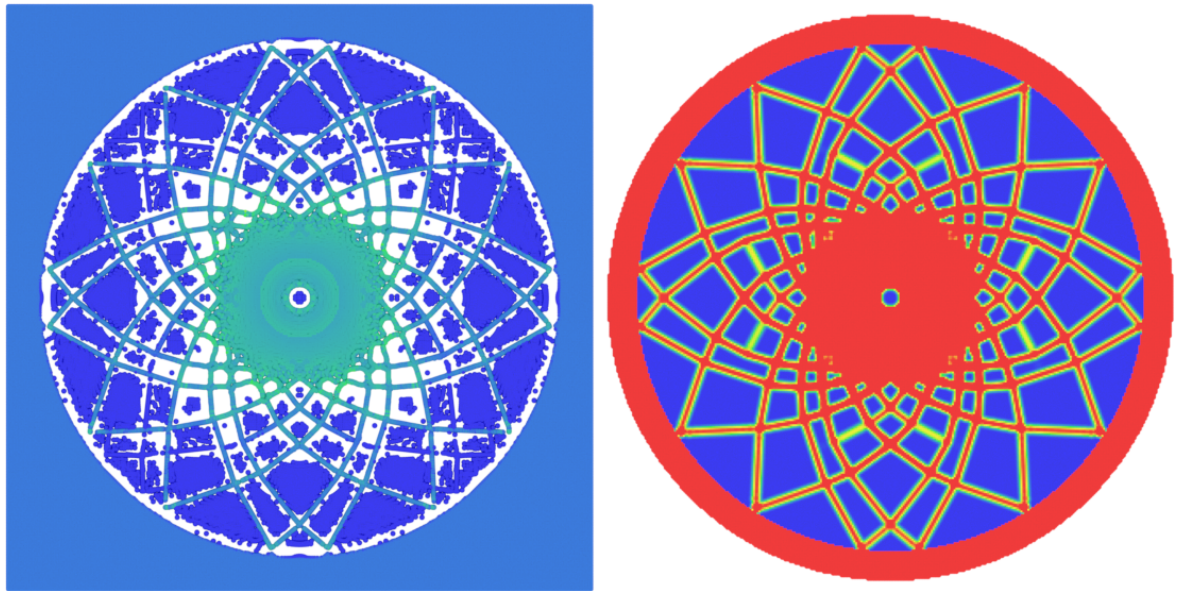


Figure 12: Circle with multiple tangential loads. The square design domain is discretized by 200×200 grid cells.

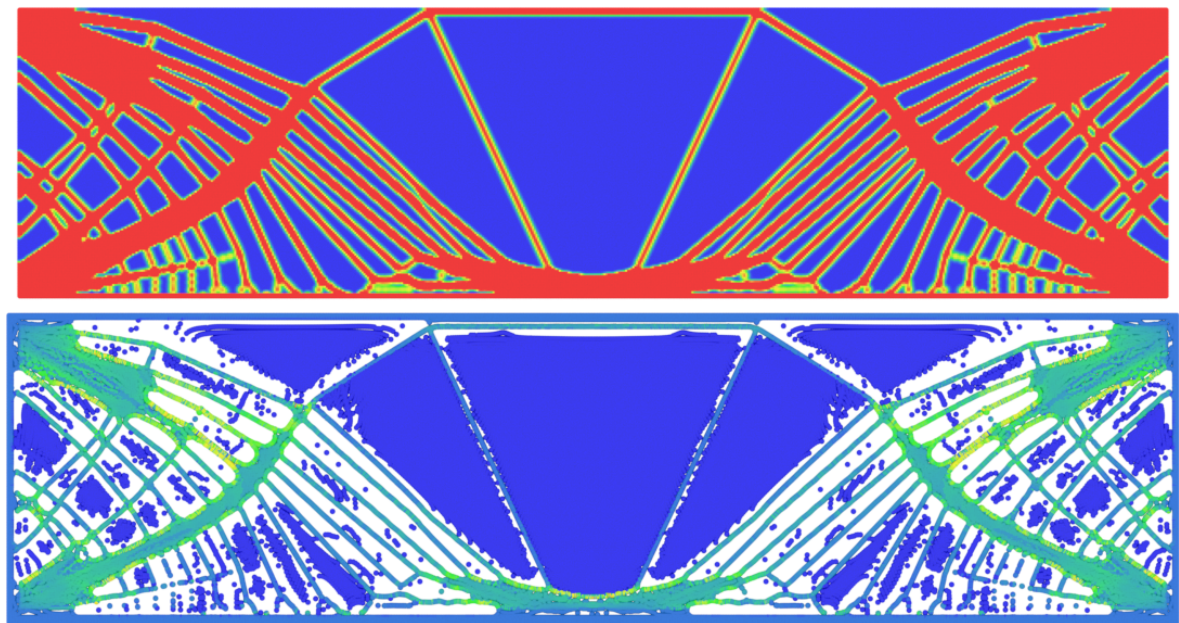


Figure 13: Bridge example. Left and right most grid nodal position is fixed. Force is added uniformly on the bottom most grid nodes. This design domain is discretized by 300×100 grid cells

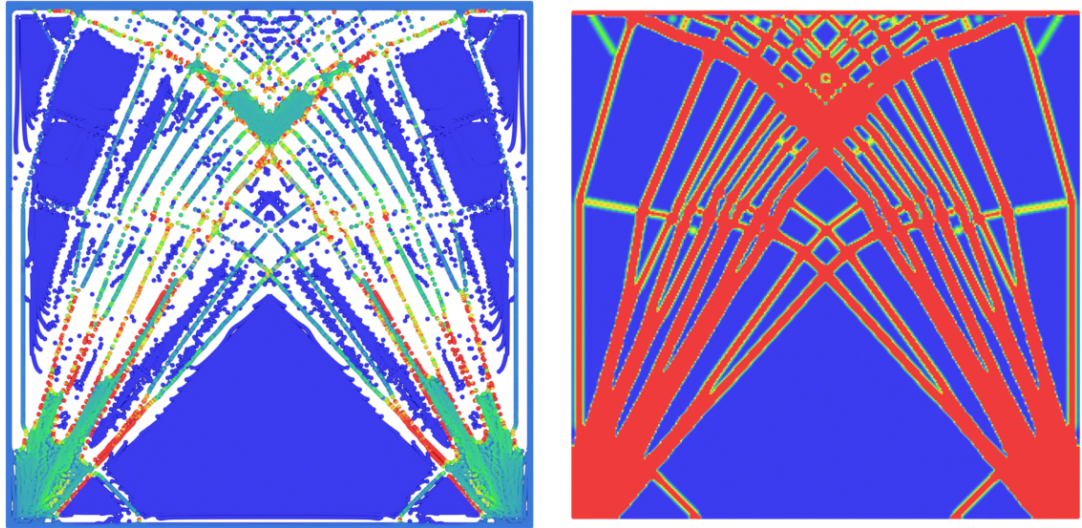


Figure 14: Plane shear example. Shear force is added uniformly on the top most grid nodes with bottom most nodes fixed. This design domain is discretized by 200 x 200 grid cells.

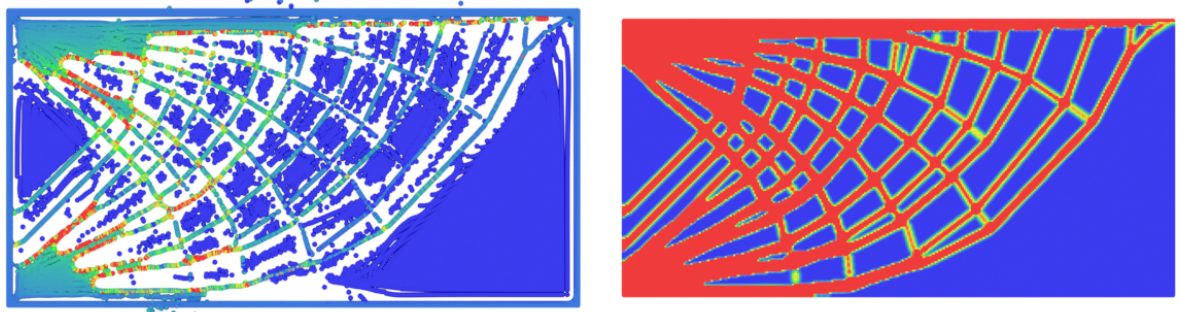


Figure 15: Plane force example. Vertical force load is added onto the topmost grid nodes while left most grid nodes are fixed. This design domain is discretized by 200 x 100 grid cells.

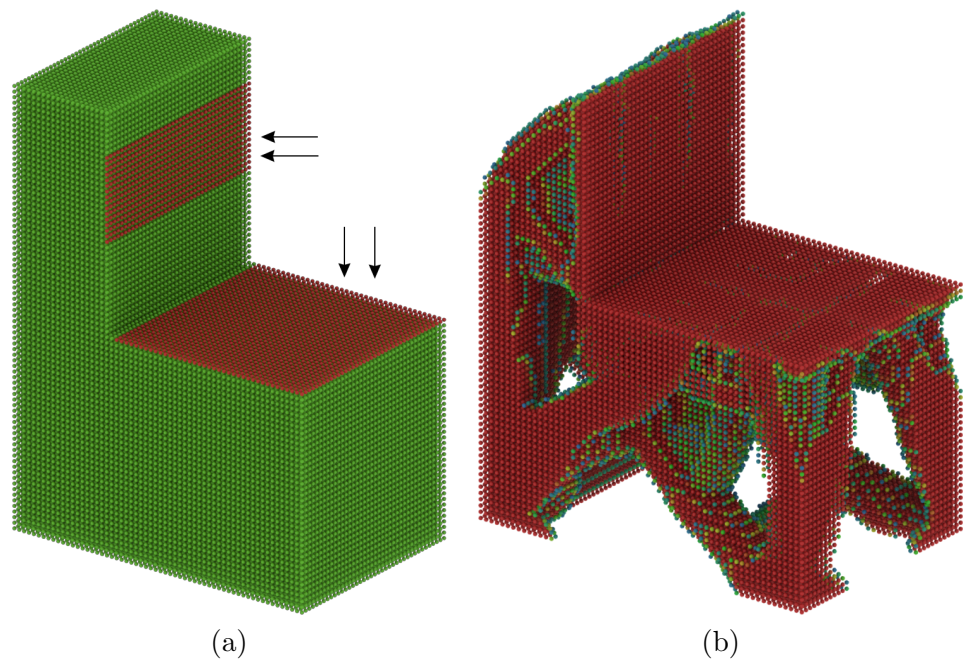


Figure 16: Low-resolution three-dimensional chair example. Force loads are demonstrated by the black arrow on the left image.

6.2. Benchmark Comparisons

In this section, the comparison of the proposed method is compared to the classic SIMP algorithm. Since the objective energy is defined slightly differently with the material point method and finite element method, the MPM version of the SIMP method is implemented and used during evaluation for a fair comparison. A benchmark consists of different loads, boundary conditions, and target volume fraction is built to compare the proposed method with SIMP. Please refer to the appendix for the optimal material distribution, volume fraction constraint, and compliance value of all experiments.

6.2.1. MPM SIMP

The MPM SIMP used in this thesis is aiming to match the FEM SIMP as closely as possible, ensuring the only difference is the simulation solver. The design variable, in this case, is the density of quadrature points. The same number of quadrature points per simulation cell is placed at the same location as in the hybrid method. With the SIMP method, each cell shares one volume, so four quadrature points inside a simulation cell are set to have the same gradient for filtering. The gradients of these four quadrature points are set to be the summation of their gradient.

6.2.2. Comparisons

As demonstrated in 17, proposed method is generally better than SIMP. With four quadrature points per simulation grid cell influence by moving carrier particles, the proposed method can achieve a more accurate single-cell structure. This is particularly helpful in alleviating jagged edges problem with the standard SIMP method. This hybrid method is considered to be more beneficial for lower volume fraction constraint, which is more favored in general manufacturing design(Fig. 18). With the removal and redistribution method accelerated with heuristic, large solid chunks are more likely to form. Besides, unlike SIMP, which filtering techniques are acted on gradients as a separate step, the proposed method implicitly encoded the filtering with spherical kernel explicitly included in objective function formulation.

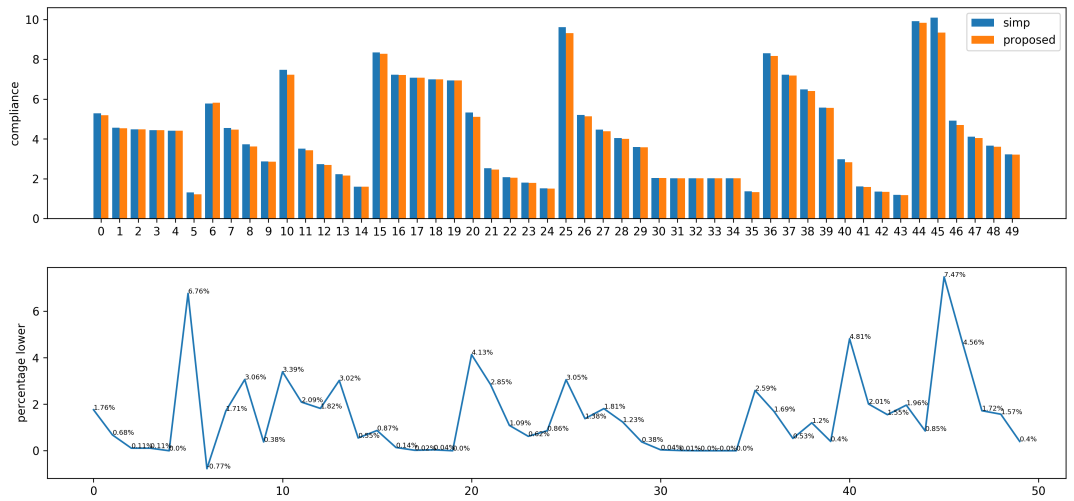


Figure 17: Benchmark comparison with state-of-the-art SIMP method. Bar chart in the first row plots the compliance for both two methods. Second row plots the relative percentage that the proposed method is lower than SIMP.

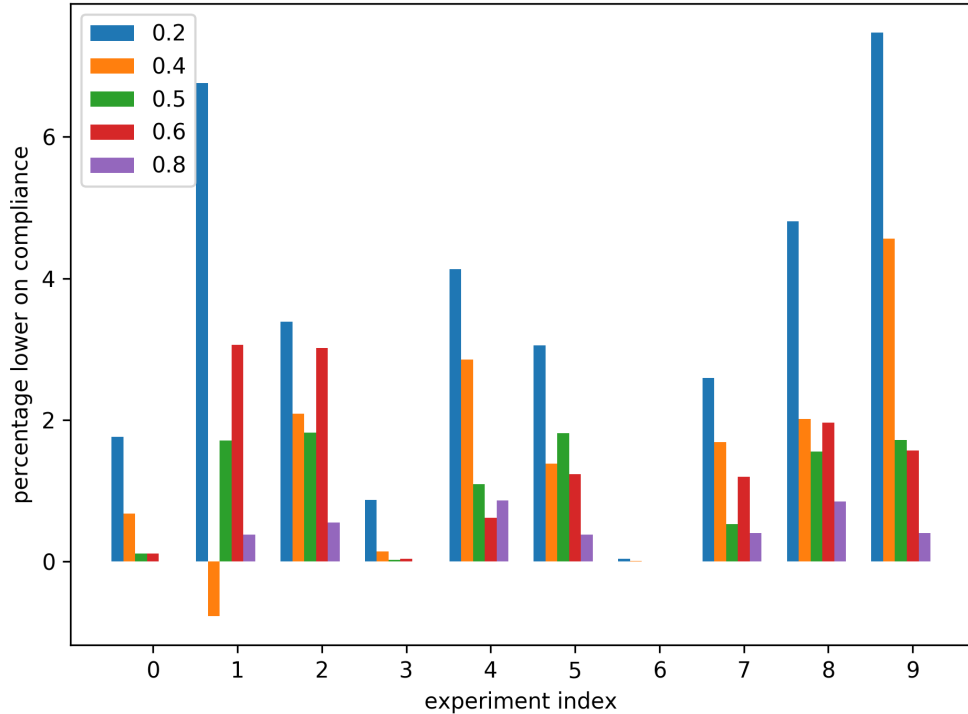


Figure 18: Compliance comparison grouped by volume. As demonstrated in this figure the proposed method show more advantage given less volume fraction constraint.

6.3. Ablation Study

6.3.1. Regularization on Optimization Variables

In the implementation of this thesis, there is no position constraint for the position of carrier particles. They are free to move away from the design domain, and if it were the case, the derivative of these particles would be zero when they are outside the kernel range of the border quadrature points. However, it is noticed in practice that the MMA optimizer is unstable in this case. To facilitate the optimization process, the maximum and the minimum step that each particle can take is restricted by enforcing a box constraint at each iteration step. Each particle can move as much as ten times the simulation grid spacing. The effectiveness of adding step size constraint on both x_p and ρ_p is shown here. Note that at the starting point of both methods with regularization, the energy is very unstable. Later in the process of optimization, the energy starts to vibrate and finally converged to a higher compliance local minima. The final compliance for proposed method, regularize x_p step size, and regularize ρ_p step size are 20.250098, 20.254920, 20.263705 respectively. The final volume fraction for these three methods is 0.299995, 0.297106, 0.299957, respectively.

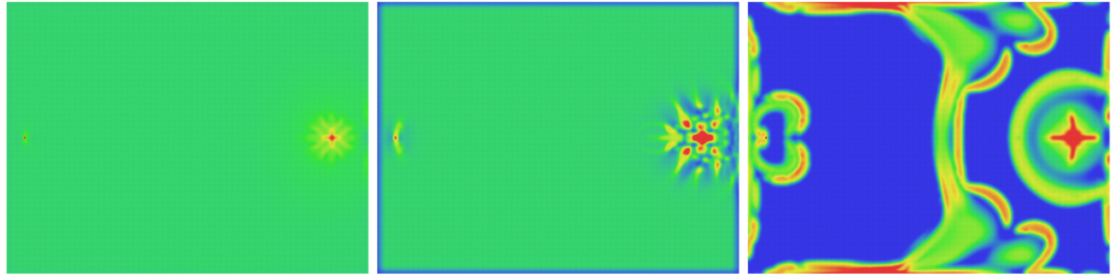


Figure 19: Comparison with proposed method and remove step size constraint on x_p and ρ_p at third iteration. Left most is proposed method with step size constraint on both x_p and ρ_p , middle image is remove step size constraint on x_p , right most image is remove step size constraint on ρ_p .

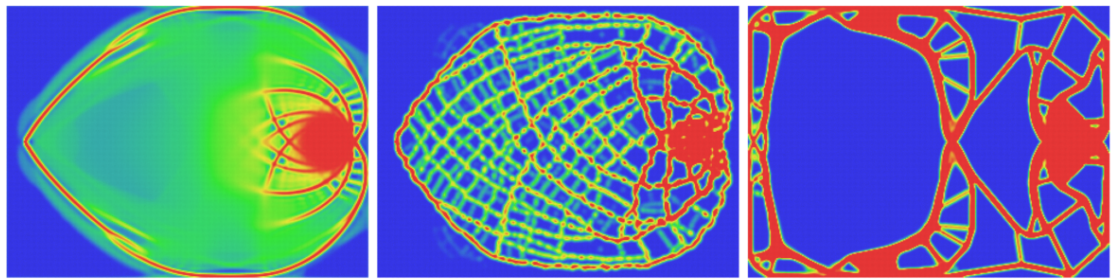


Figure 20: Comparison with proposed method and remove step size constraint on x_p and ρ_p at 40th iteration.

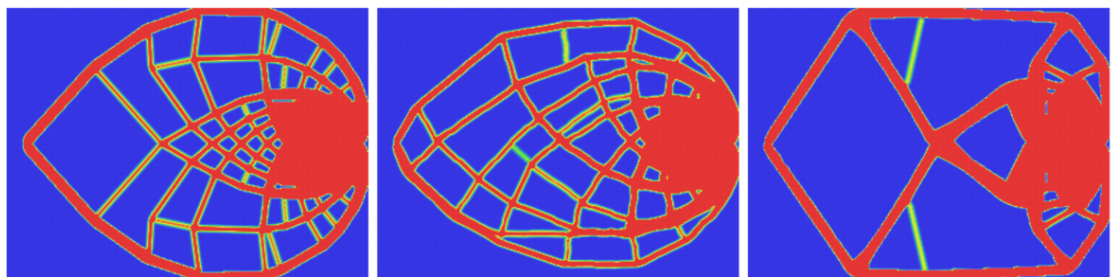


Figure 21: Comparison with proposed method and remove step size constraint on x_p and ρ_p at final state.

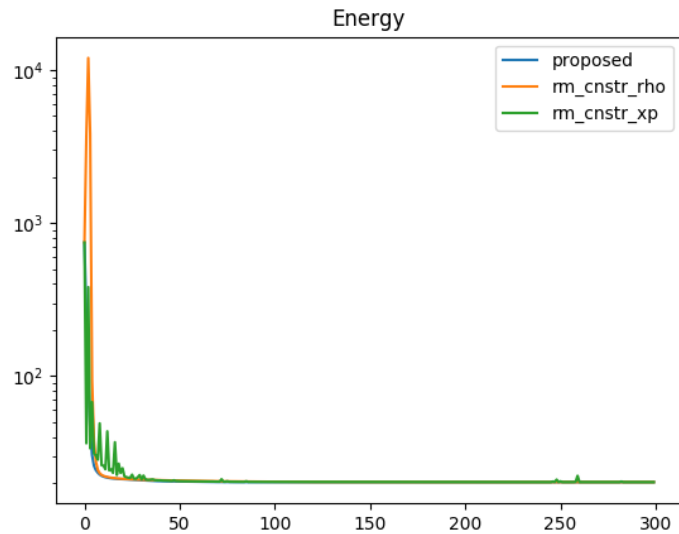


Figure 22: Objective energy plot of proposed method and remove step size constraint on either x_p or ρ_p . Note that at first couple of iterations those do not have constraint on step size experienced large energy variation, resulting in higher compliance local minima.

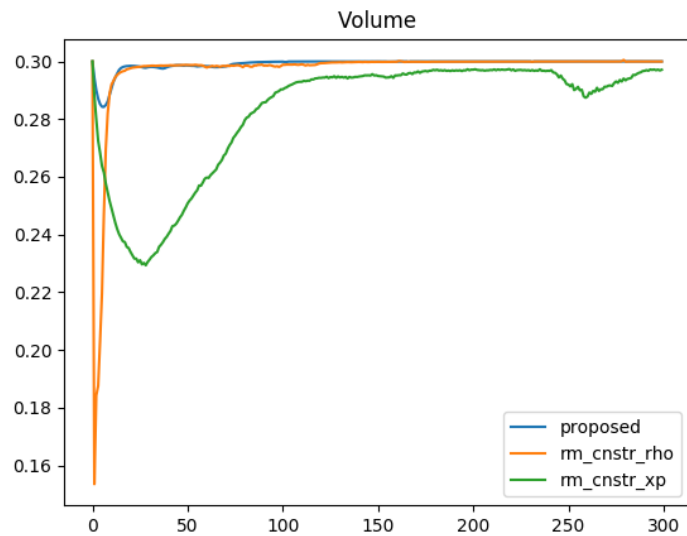


Figure 23: Volume plot of proposed method and remove step size constraint on either x_p or ρ_p . Without constraint on step size volume constraint satisfaction is also unstable.

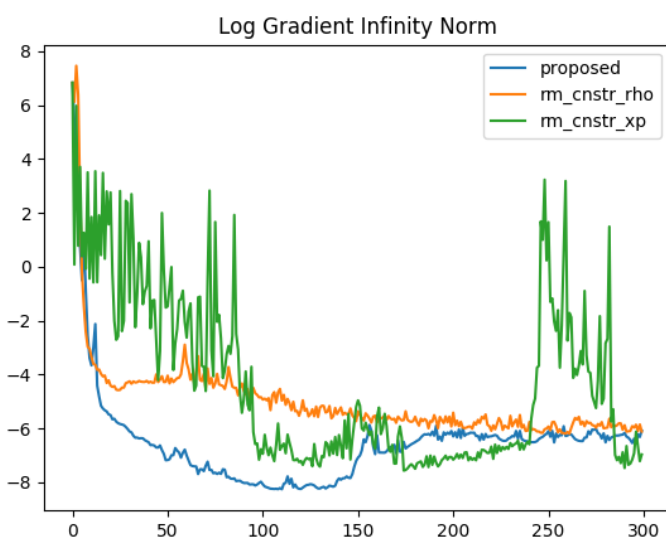


Figure 24: Gradient infinity norm plot of proposed method and remove step size constraint on either x_p or ρ_p .

6.3.2. Wrapper Function on Density at Quadrature Points

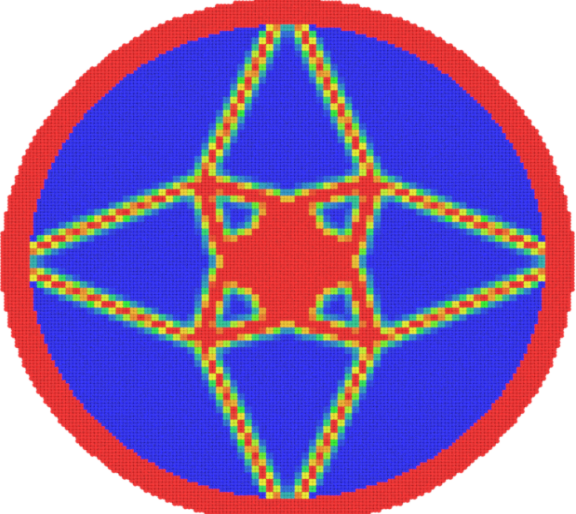
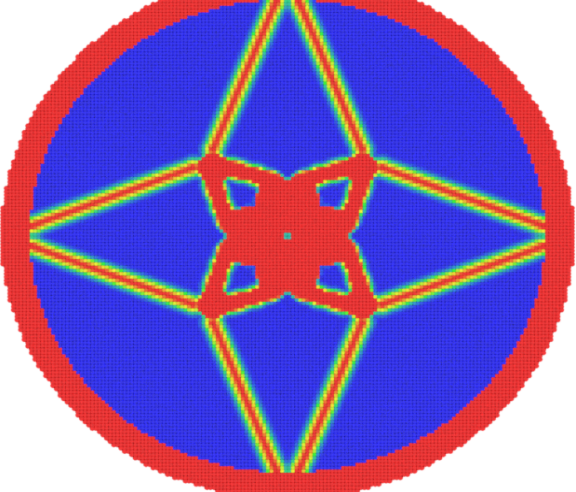
As it is aforementioned, a wrapper function must exist to ensure the density value on quadrature points remains between 0 to 1. This is important in two folds. Firstly, the final material density should be within 0 to 1 to ensure the existence of such material in real life. Secondly, forming harder material, namely, higher Young's modulus, is able to achieve lower compliance. Both gathering of particles and raising the density of each particle to infinity can give harder material. Removing the wrapper function basically causes the optimization problem itself to be ill-defined. It appears to be multiple choices on the wrapper function as long as it regularizes the density to be 0 to 1. The wrapper function in this thesis is linear, for the most part. It would be very intriguing to see other wrapper function such as a sigmoid function to better map the density value to either 0 or 1 to achieve binary results without post-processing.

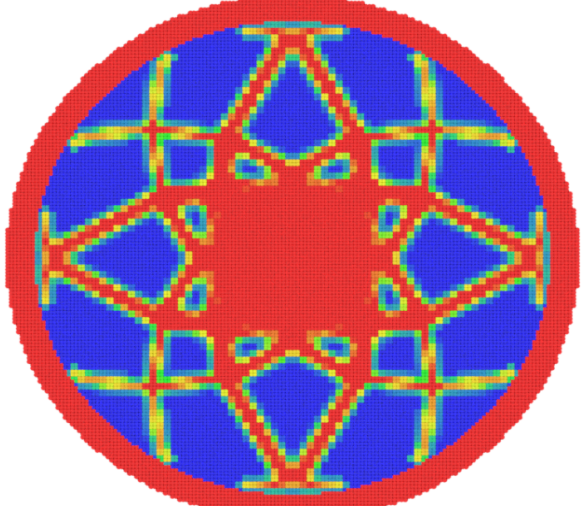
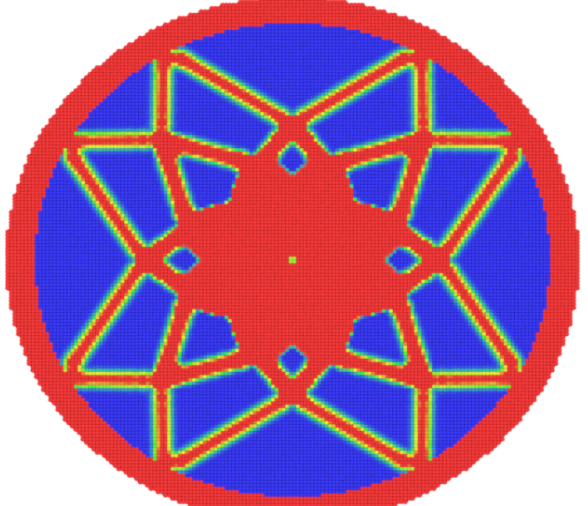
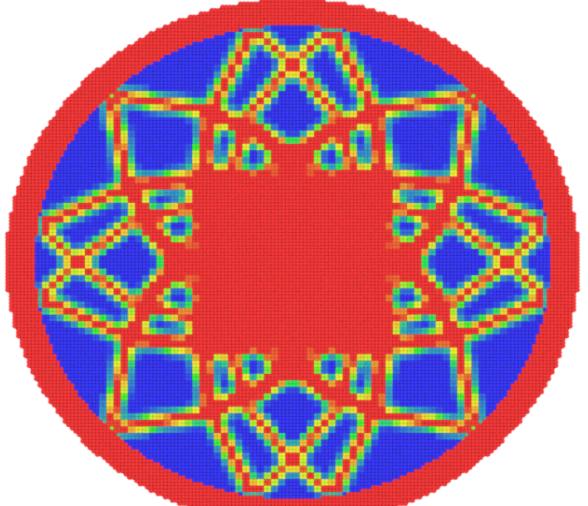
CHAPTER 7 : Conclusion and Outlook

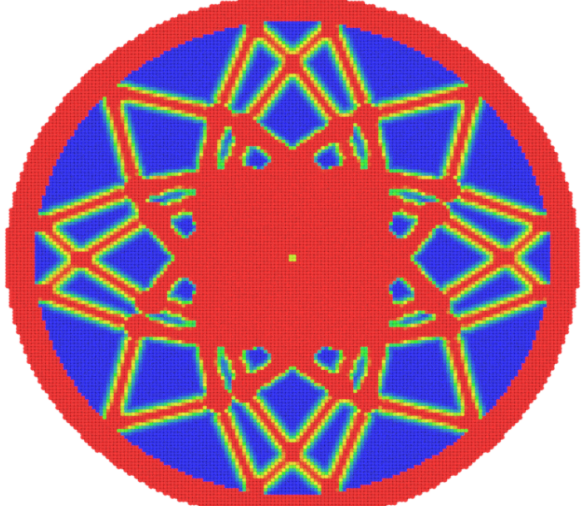
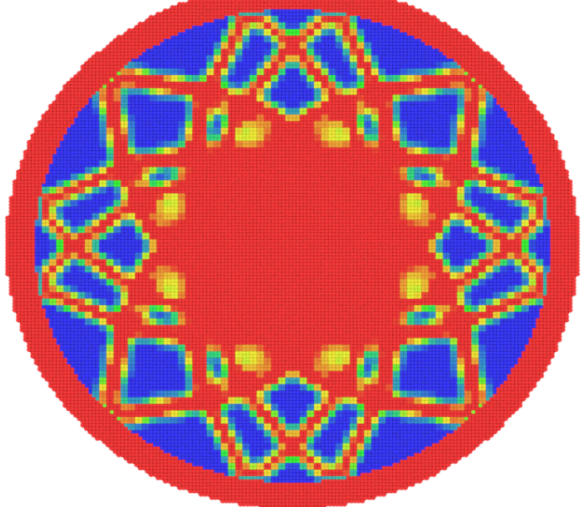
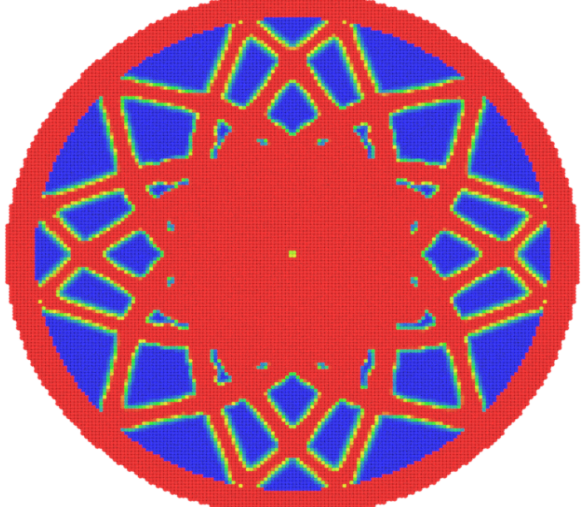
This thesis presents the first material point method based optimization framework for structural compliance minimization in the field of topology optimization. The choice of selecting suitable design variables is discussed. The objective derivation using MPM, as well as the stiffness matrix assembling process, are given. Highly detailed geometry features could be seen from the various optimal material distribution obtained by the proposed method, and a comparison with the state-of-the-art method is evaluated on a large benchmark to endorse the contribution of this method.

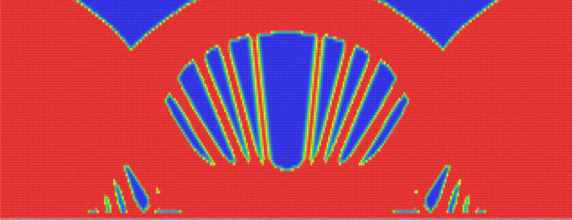
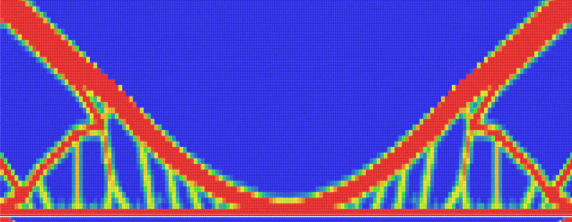
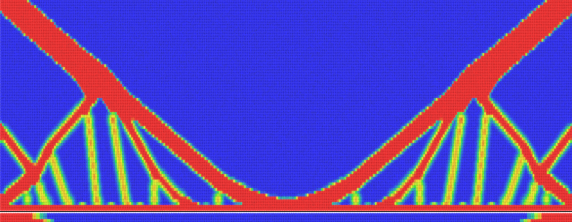
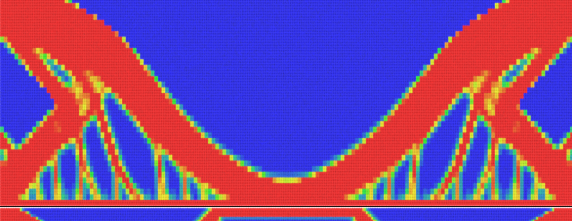
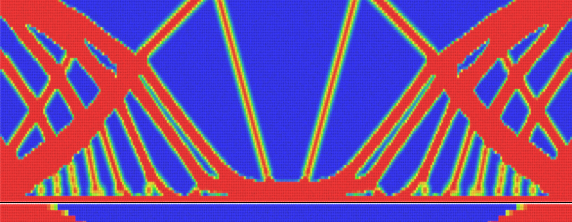
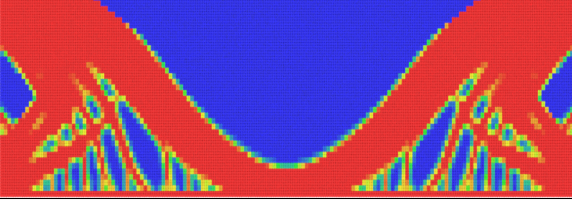
The author would like to investigate the possibilities of the second-order method further. One possible direction is to use only the diagonal entry of K^{-1} and use this matrix instead of an identity matrix to perform L-BFGS. In this thesis, the step size is constrained to regularize the optimizer, it would be interesting to see if optimize x_p and ρ_p of carrier particles alternately is a better choice. The author also intends to improve the performance of the current code base to account for higher resolution results to further validate the current results. In addition, most results in this thesis are two-dimensional. It is definitely future work to validate the proposed method in three-dimensional cases. Non-linear elasticity will also be explored in the future.

APPENDIX

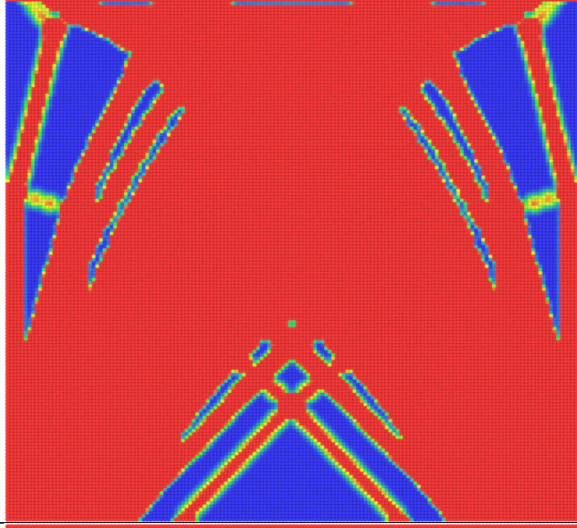
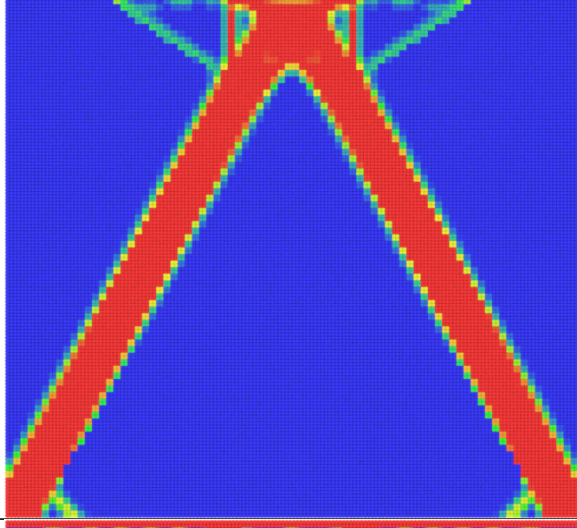
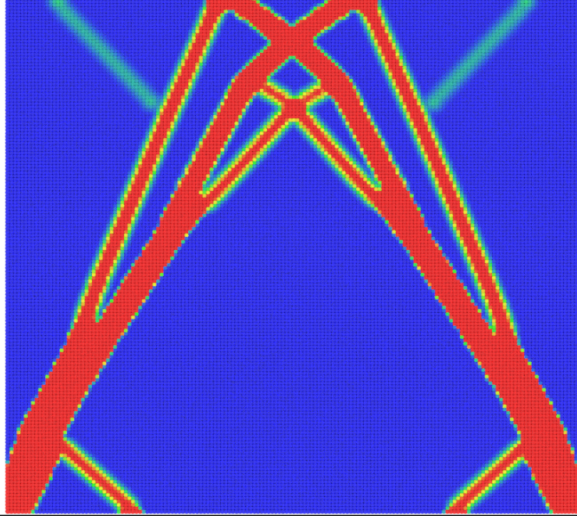
result	method	compliance	volume fraction
	SIMP	52.816682	0.2
	Proposed (1.76 percent lower)	51.885357	0.2

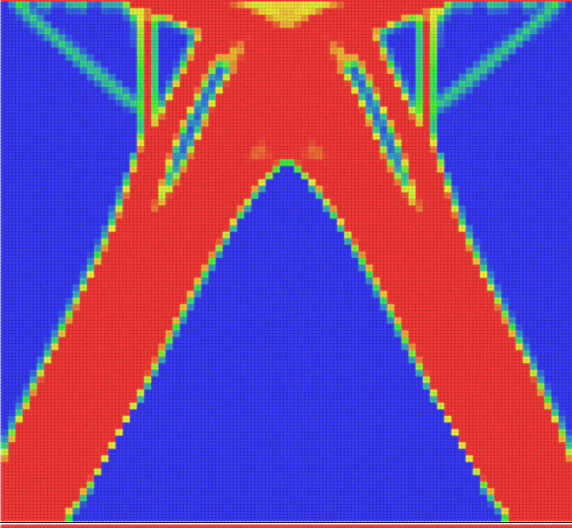
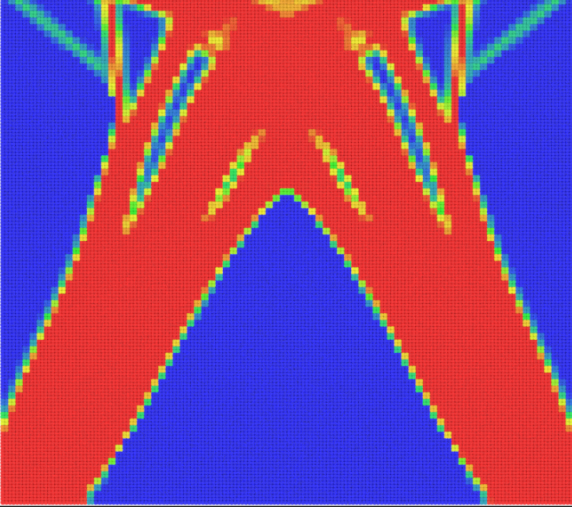
	SIMP	45.691887	0.4
	Proposed (0.68 percent lower)	45.381079	0.4
	SIMP	44.799977	0.5

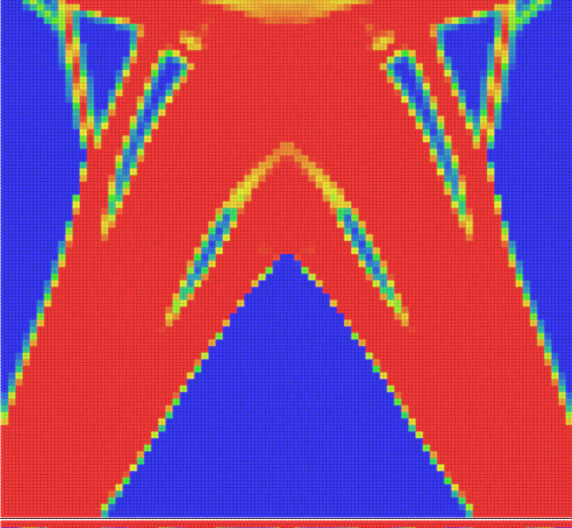
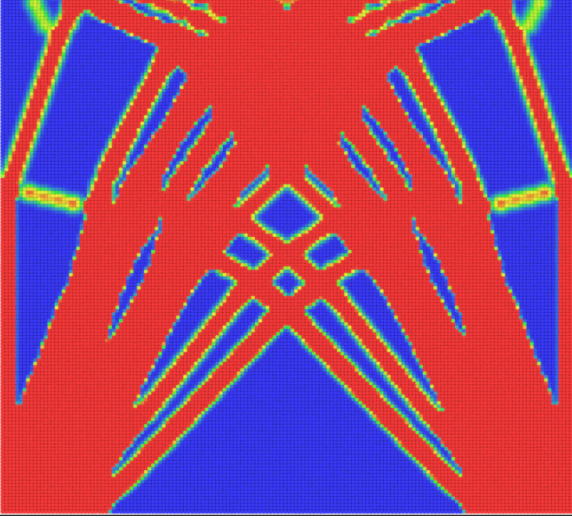
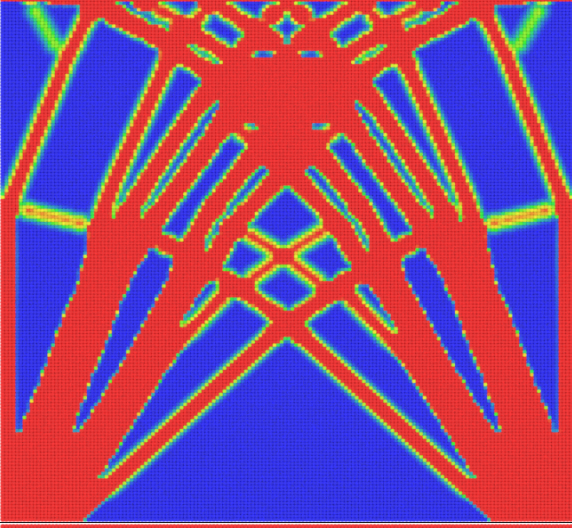
	Proposed (0.11 percent lower)	44.748975	0.5
	SIMP	44.38794	0.6
	Proposed (0.11 percent lower)	44.340948	0.6

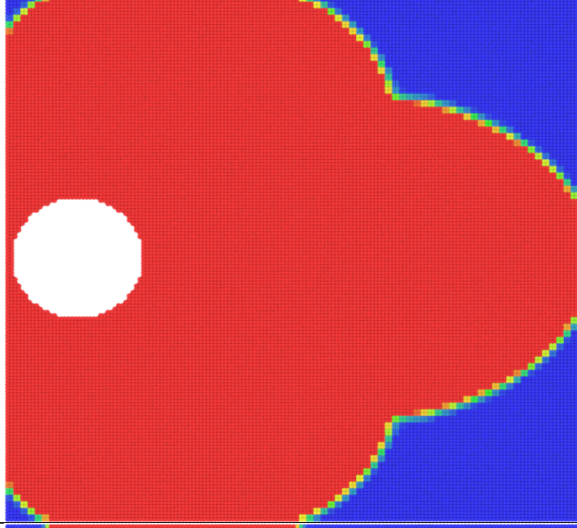
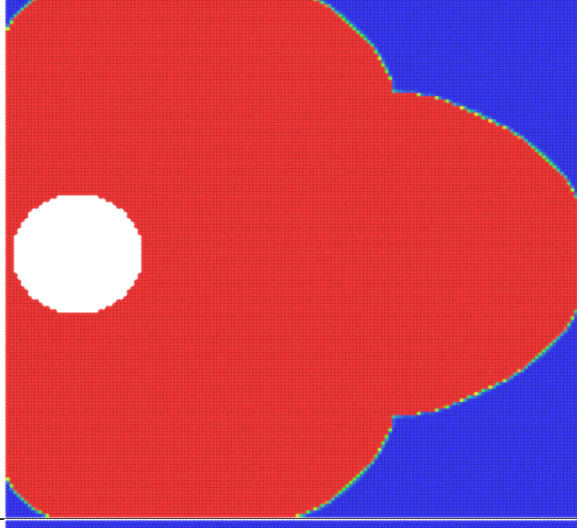
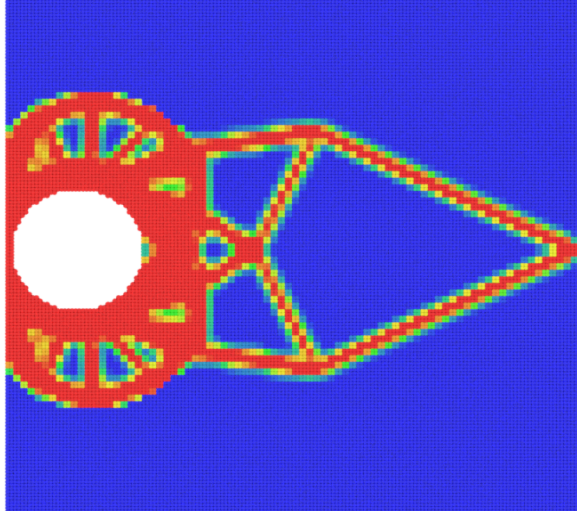
	SIMP	44.059963	0.8
	Proposed (0.0 percent lower)	44.058612	0.8
	SIMP	0.130592	0.2
	Proposed (6.76 percent lower)	0.121762	0.2
	SIMP	0.057744	0.4
	Proposed (-0.77 percent lower)	0.05819	0.4
	SIMP	0.045443	0.5

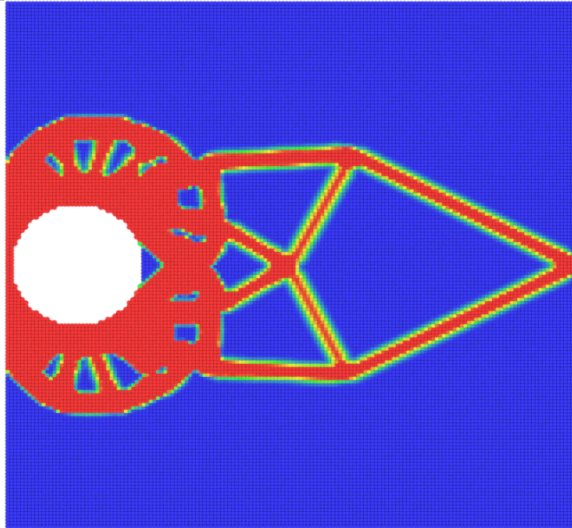
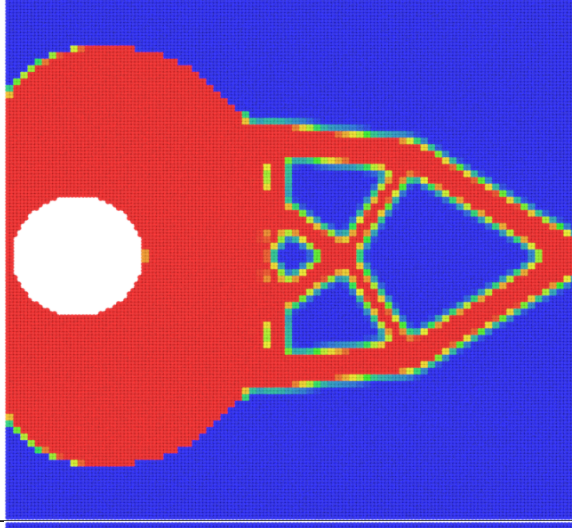
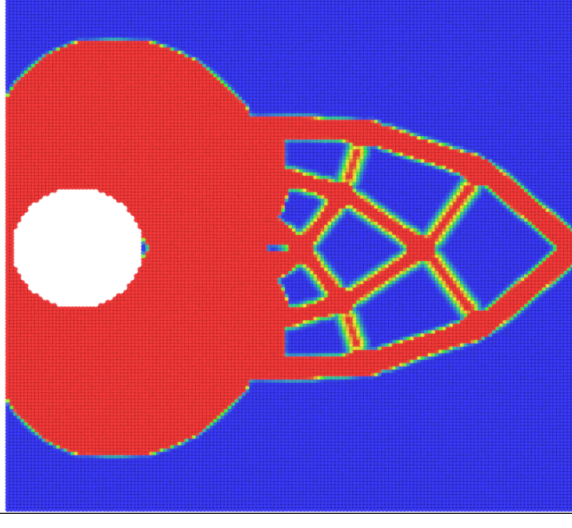
	Proposed (1.71 percent lower)	0.044667	0.5
	SIMP	0.037301	0.6
	Proposed (3.06 percent lower)	0.036161	0.6
	SIMP	0.028713	0.8

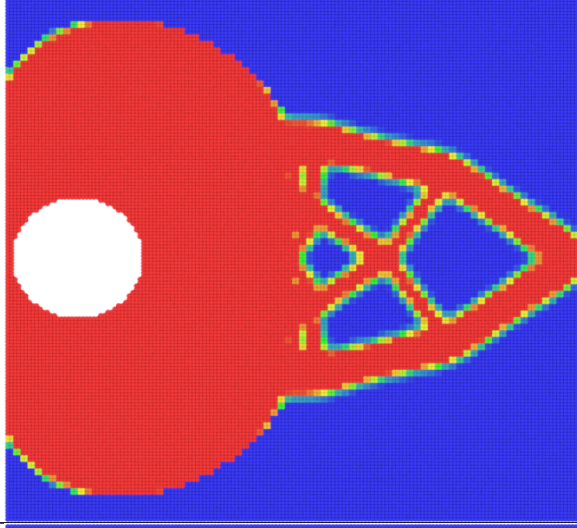
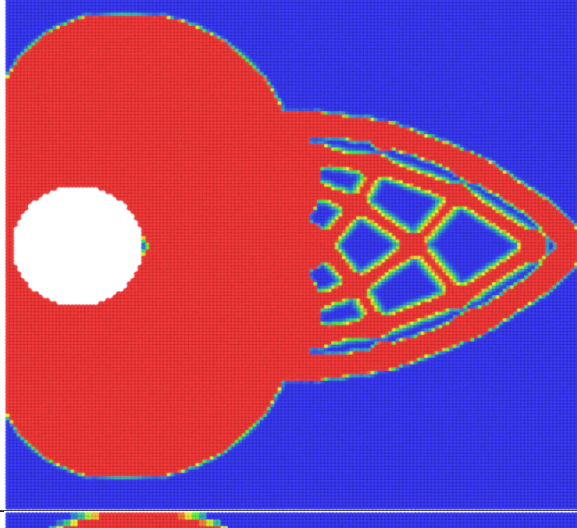
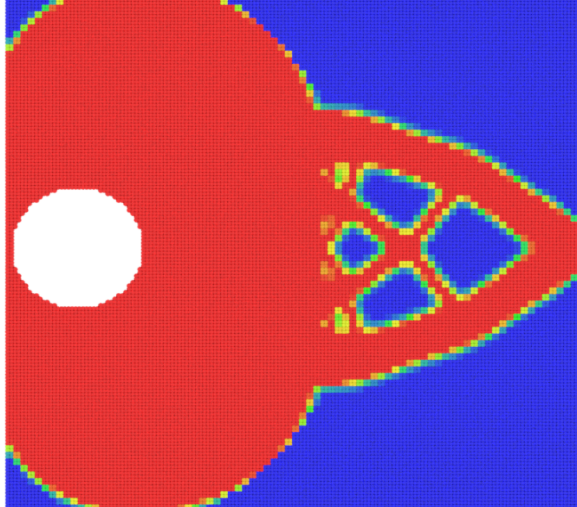
	Proposed (0.38 percent lower)	0.028603	0.8
	SIMP	0.747746	0.2
	Proposed (3.39 percent lower)	0.722428	0.2

	SIMP	0.350606	0.4
	Proposed (2.09 percent lower)	0.343273	0.4
	SIMP	0.273565	0.5

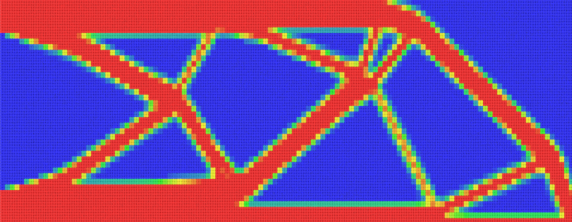
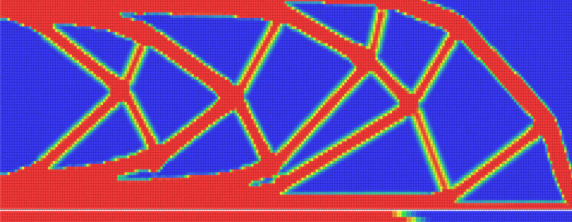
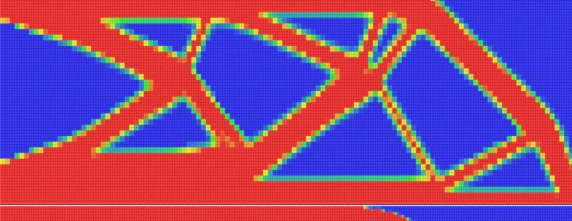
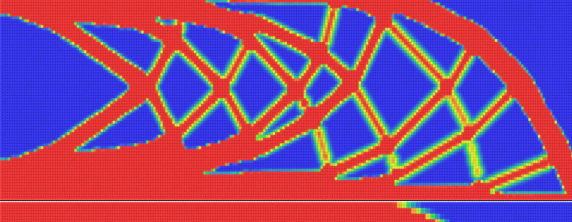
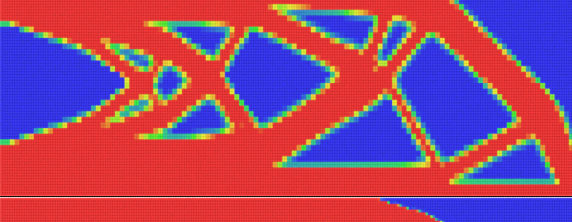
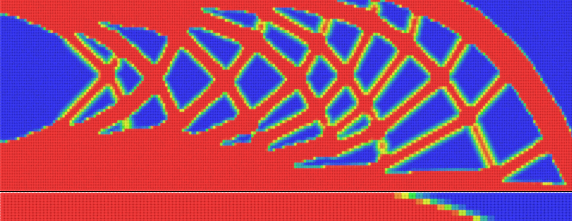
	Proposed (1.82 percent lower)	0.268594	0.5
	SIMP	0.222295	0.6
	Proposed (3.02 percent lower)	0.21558	0.6

	SIMP	0.160492	0.8
	Proposed (0.55 percent lower)	0.159605	0.8
	SIMP	0.835149	0.2

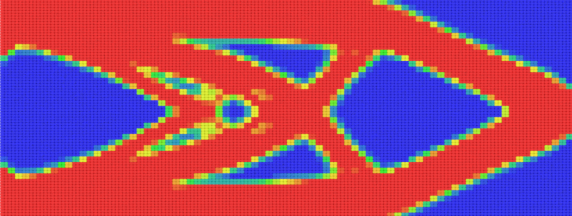
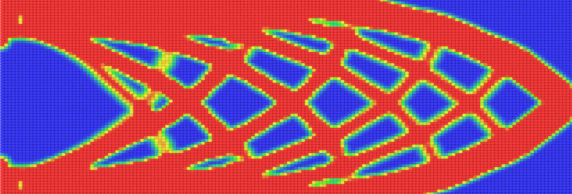
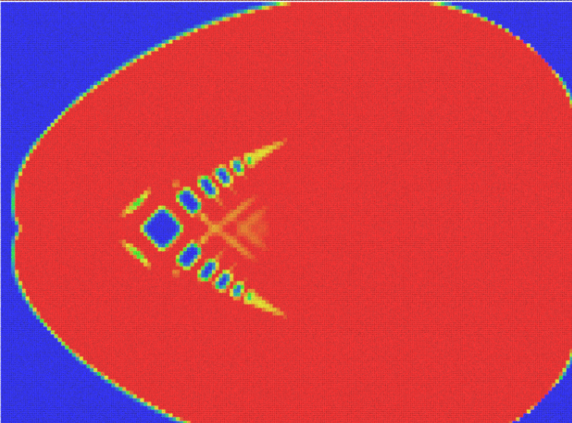
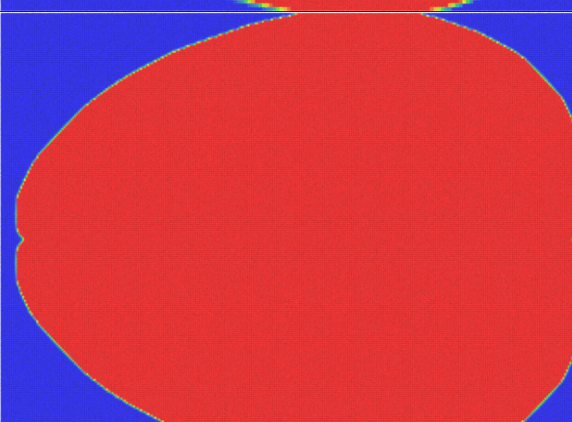
	Proposed (0.87 percent lower)	0.827895	0.2
	SIMP	722.36498	0.4
	Proposed (0.14 percent lower)	721.335234	0.4

	SIMP	707.866543	0.5
	Proposed (0.02 percent lower)	707.700581	0.5
	SIMP	699.989381	0.6

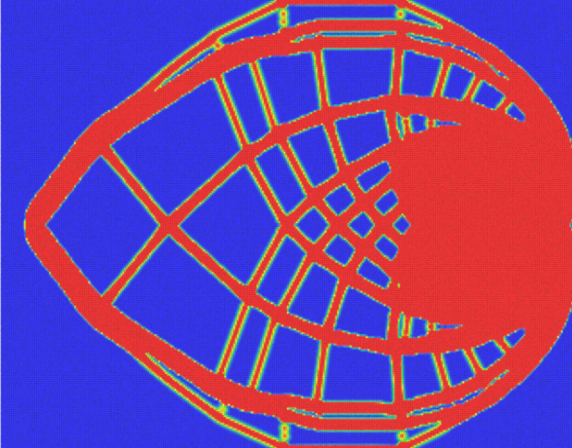
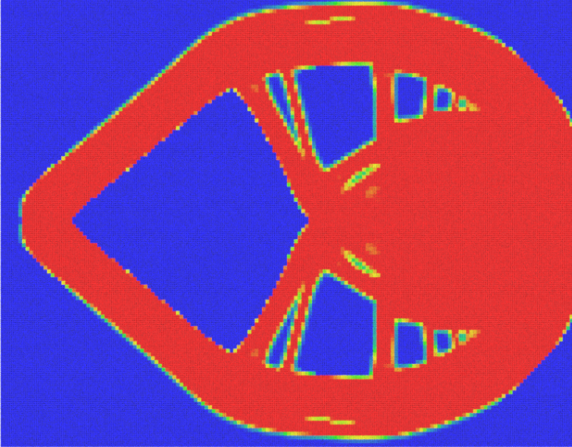
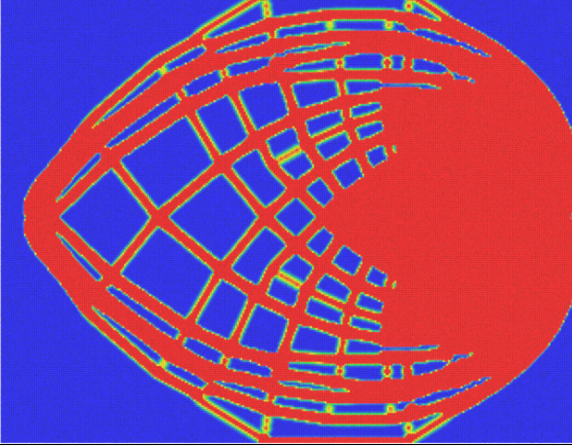
	Proposed (0.04 percent lower)	699.708589	0.6
	SIMP	694.322436	0.8
	Proposed (0.0 percent lower)	694.294487	0.8
	SIMP	53.276943	0.2
	Proposed (4.13 percent lower)	51.079255	0.2

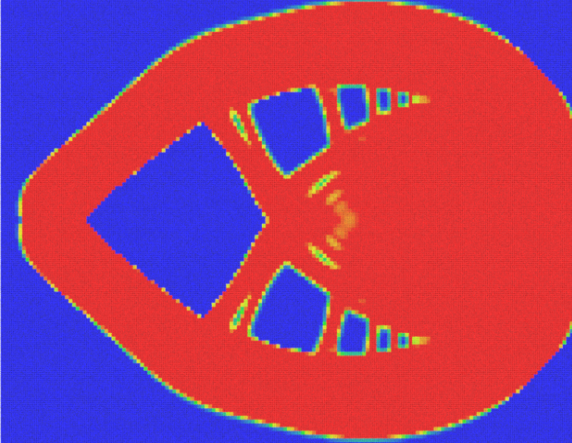
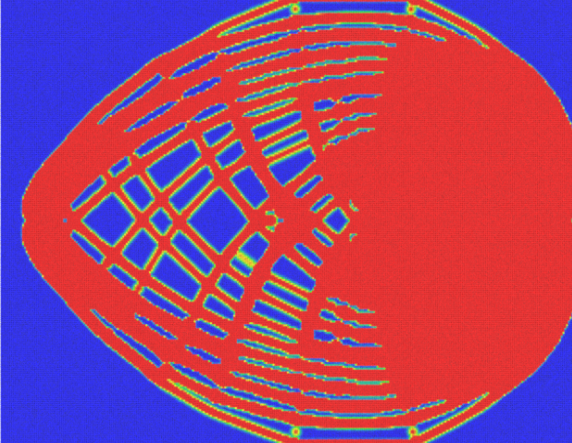
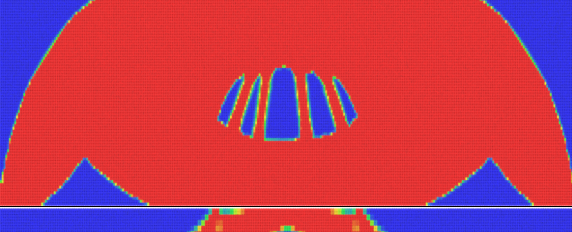
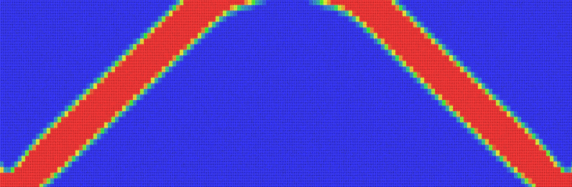
	SIMP	25.303766	0.4
	Proposed (2.85 percent lower)	24.582622	0.4
	SIMP	20.738051	0.5
	Proposed (1.09 percent lower)	20.511702	0.5
	SIMP	18.024105	0.6
	Proposed (0.62 percent lower)	17.912285	0.6
	SIMP	15.098509	0.8

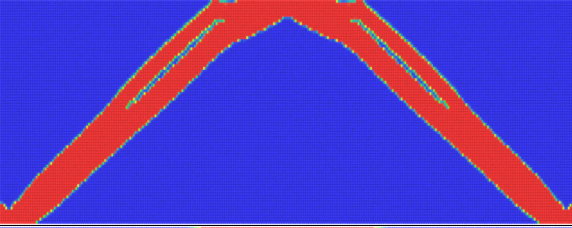
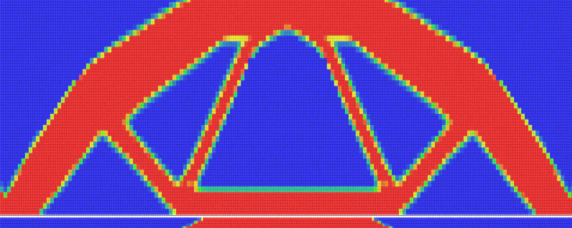
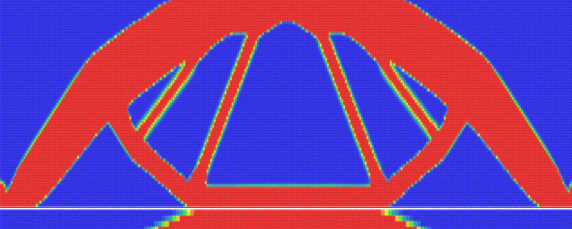
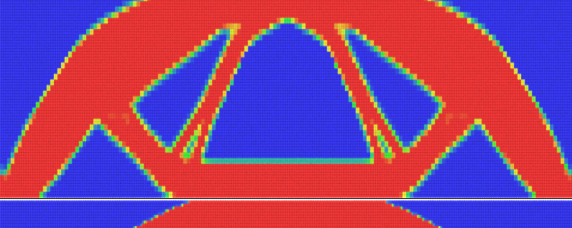
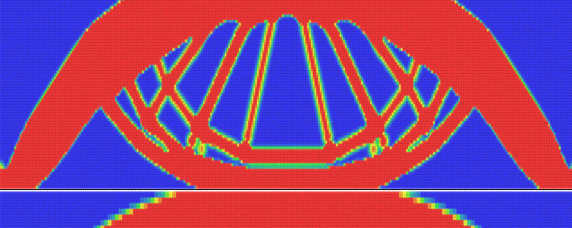
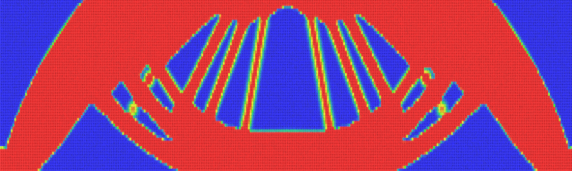
	Proposed (0.86 percent lower)	14.968832	0.8
	SIMP	96.164589	0.2
	Proposed (3.05 percent lower)	93.229702	0.2
	SIMP	52.103176	0.4
	Proposed (1.38 percent lower)	51.386536	0.4
	SIMP	44.671684	0.5
	Proposed (1.81 percent lower)	43.864173	0.5

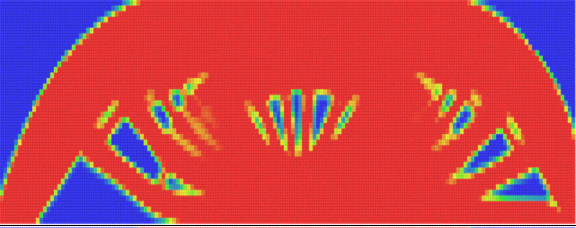
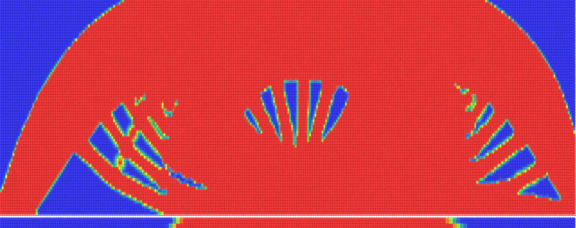
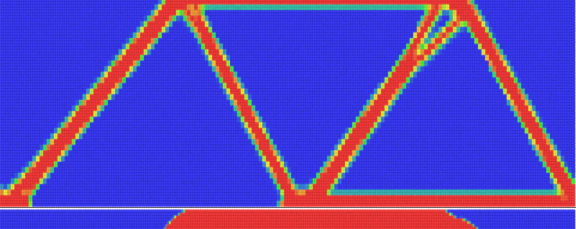
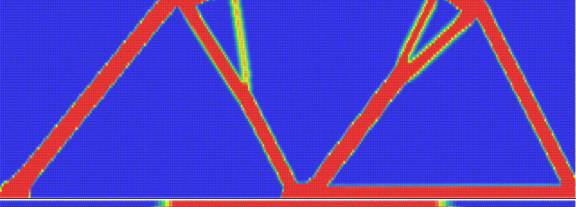
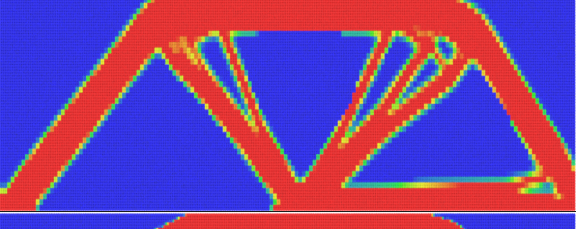
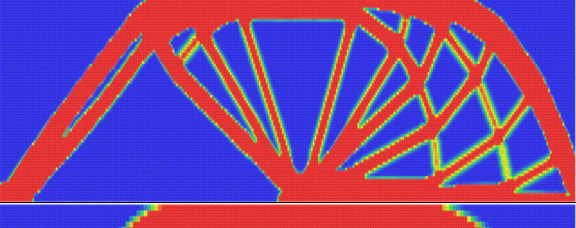
	SIMP	40.47109	0.6
	Proposed (1.23 percent lower)	39.972655	0.6
	SIMP	35.924993	0.8
	Proposed (0.38 percent lower)	35.789661	0.8

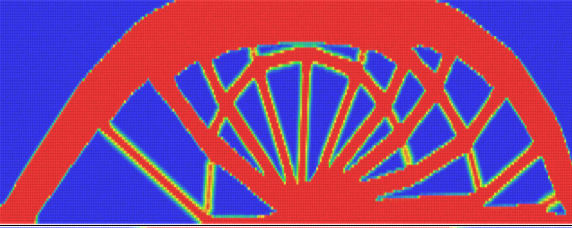
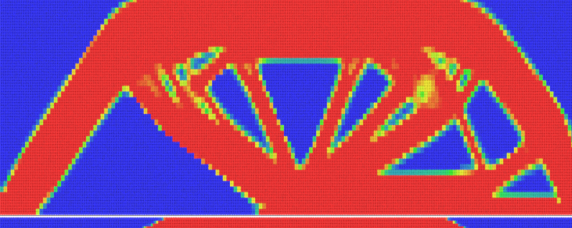
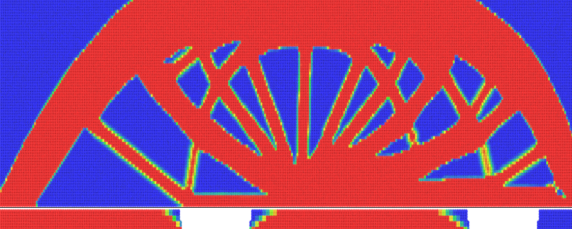
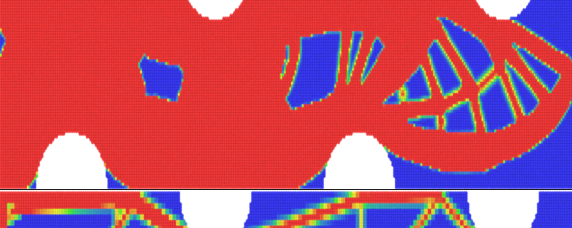
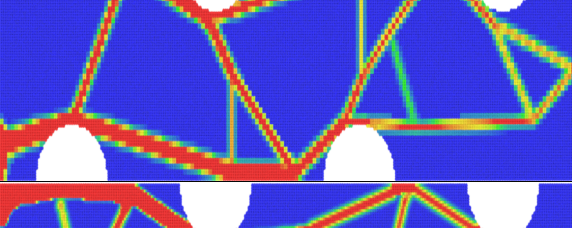
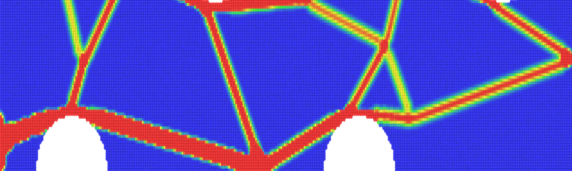
	SIMP	20.374609	0.2
	Proposed (0.04 percent lower)	20.366757	0.2
	SIMP	20203.180984	0.4

	Proposed (0.01 percent lower)	20201.986064	0.4
	SIMP	20182.57285	0.5
	Proposed (-0.0 percent lower)	20182.681955	0.5

	SIMP	20171.621661	0.6
	Proposed (-0.0 percent lower)	20172.038534	0.6
	SIMP	20162.336249	0.8
	Proposed (0.0 percent lower)	20162.23289	0.8
	SIMP	135.986019	0.2

	Proposed (2.59 percent lower)	132.464016	0.2
	SIMP	83.05857	0.4
	Proposed (1.69 percent lower)	81.658157	0.4
	SIMP	72.273674	0.5
	Proposed (0.53 percent lower)	71.890067	0.5
	SIMP	64.868354	0.6
	Proposed (1.2 percent lower)	64.087811	0.6

	SIMP	55.777313	0.8
	Proposed (0.4 percent lower)	55.556346	0.8
	SIMP	29.727487	0.2
	Proposed (4.81 per- cent lower)	28.296551	0.2
	SIMP	16.148999	0.4
	Proposed (2.01 per- cent lower)	15.825183	0.4
	SIMP	13.584667	0.5

	Proposed (1.55 percent lower)	13.374522	0.5
	SIMP	11.923911	0.6
	Proposed (1.96 percent lower)	11.690681	0.6
	SIMP	9.919943	0.8
	Proposed (0.85 percent lower)	9.835819	0.8
	SIMP	1.009705	0.2
	Proposed (7.47 percent lower)	0.934233	0.2

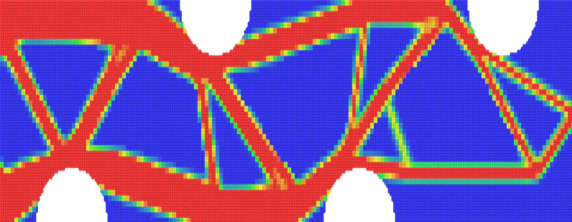
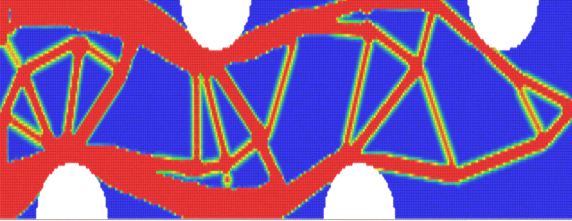
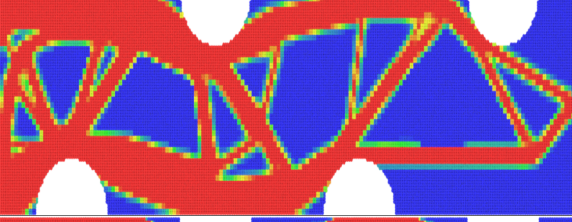
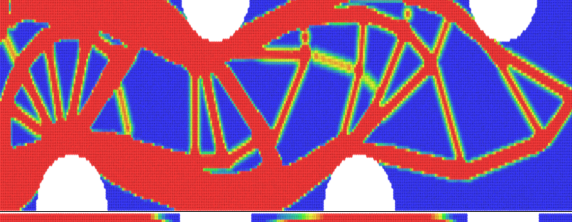
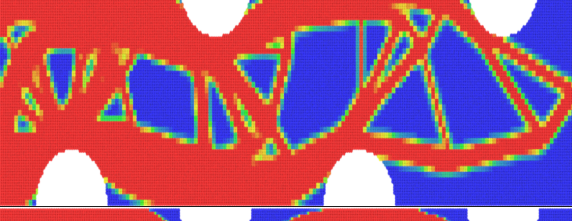
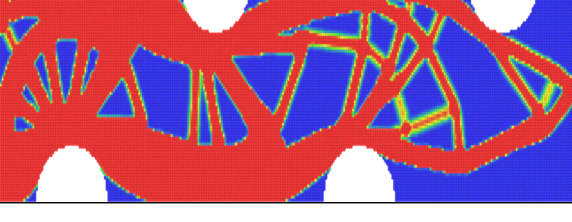
	SIMP	491.983649	0.4
	Proposed (4.56 percent lower)	469.572364	0.4
	SIMP	411.363017	0.5
	Proposed (1.72 percent lower)	404.272524	0.5
	SIMP	366.55917	0.6
	Proposed (1.57 percent lower)	360.813628	0.6

Table 1: Benchmark results and compliance values

Bibliography

- Niels Aage, Erik Andreassen, Boyan S Lazarov, and Ole Sigmund. 2017. Giga-voxel computational morphogenesis for structural design. *Nature* 550, 7674 (2017), 84.
- Grégoire Allaire, François Jouve, and Anca-Maria Toader. 2004. Structural optimization using sensitivity analysis and a level-set method. *Journal of computational physics* 194, 1 (2004), 363–393.
- Ted Belytschko, Yury Krongauz, Daniel Organ, Mark Fleming, and Petr Krysl. 1996. Meshless methods: an overview and recent developments. *Computer methods in applied mechanics and engineering* 139, 1-4 (1996), 3–47.
- Martin P Bendsøe. 1989. Optimal shape design as a material distribution problem. *Structural optimization* 1, 4 (1989), 193–202.
- Martin Philip Bendsøe and Noboru Kikuchi. 1988. Generating optimal topologies in structural design using a homogenization method. *Computer methods in applied mechanics and engineering* 71, 2 (1988), 197–224.
- Yu Fang, Minchen Li, Ming Gao, and Chenfanfu Jiang. 2019. Silly rubber: an implicit material point method for simulating non-equilibrated viscoelastic and elastoplastic solids. *ACM Transactions on Graphics (TOG)* 38, 4 (2019), 118.
- Xu Guo, Weisheng Zhang, and Wenliang Zhong. 2014. Doing topology optimization explicitly and geometrically—a new moving morphable components based framework. *Journal of Applied Mechanics* 81, 8 (2014), 081009.
- Chenfanfu Jiang, Craig Schroeder, Joseph Teran, Alexey Stomakhin, and Andrew Selle. 2016. The material point method for simulating continuum materials. In *ACM SIGGRAPH 2016 Courses*. ACM, 24.

- Gergely Klár, Theodore Gast, Andre Pradhana, Chuyuan Fu, Craig Schroeder, Chenfanfu Jiang, and Joseph Teran. 2016. Drucker-prager elastoplasticity for sand animation. *ACM Transactions on Graphics (TOG)* 35, 4 (2016), 103.
- Haixiang Liu, Yuanming Hu, Bo Zhu, Wojciech Matusik, and Eftychios Sifakis. 2018. Narrow-band topology optimization on a sparsely populated grid. In *SIGGRAPH Asia 2018 Technical Papers*. ACM, 251.
- K Maute and O Sigmund. 2013. Topology optimization approaches: A comparative review. *Structural and Multidisciplinary Optimization* 6 (2013).
- Anthony George Maldon Michell. 1904. LVIII. The limits of economy of material in frame-structures. *The London, Edinburgh, and Dublin Philosophical Magazine and Journal of Science* 8, 47 (1904), 589–597.
- Marek Krzysztof Misztal and Jakob Andreas Bærentzen. 2012. Topology-adaptive interface tracking using the deformable simplicial complex. *ACM Transactions on Graphics (TOG)* 31, 3 (2012), 24.
- HP Mlejnek. 1992. Some aspects of the genesis of structures. *Structural optimization* 5, 1-2 (1992), 64–69.
- Ole Sigmund. 2001. A 99 line topology optimization code written in Matlab. *Structural and multidisciplinary optimization* 21, 2 (2001), 120–127.
- Ole Sigmund. 2007. Morphology-based black and white filters for topology optimization. *Structural and Multidisciplinary Optimization* 33, 4-5 (2007), 401–424.
- Ole Sigmund and Kurt Maute. 2012. Sensitivity filtering from a continuum mechanics perspective. *Structural and Multidisciplinary Optimization* 46, 4 (2012), 471–475.
- Alexey Stomakhin, Craig Schroeder, Lawrence Chai, Joseph Teran, and Andrew Selle. 2013.

A material point method for snow simulation. *ACM Transactions on Graphics (TOG)* 32, 4 (2013), 102.

Deborah Sulsky, Shi-Jian Zhou, and Howard L Schreyer. 1995. Application of a particle-in-cell method to solid mechanics. *Computer physics communications* 87, 1-2 (1995), 236–252.

Krister Svanberg. 1987. The method of moving asymptotes—a new method for structural optimization. *International journal for numerical methods in engineering* 24, 2 (1987), 359–373.

Andre Pradhana Tampubolon, Theodore Gast, Gergely Klár, Chuyuan Fu, Joseph Teran, Chenfanfu Jiang, and Ken Museth. 2017. Multi-species simulation of porous sand and water mixtures. *ACM Transactions on Graphics (TOG)* 36, 4 (2017), 105.

Andreas Wächter and Lorenz T Biegler. 2006. On the implementation of an interior-point filter line-search algorithm for large-scale nonlinear programming. *Mathematical programming* 106, 1 (2006), 25–57.

Fengwen Wang, Boyan Stefanov Lazarov, and Ole Sigmund. 2011. On projection methods, convergence and robust formulations in topology optimization. *Structural and Multidisciplinary Optimization* 43, 6 (2011), 767–784.

Michael Yu Wang, Xiaoming Wang, and Dongming Guo. 2003. A level set method for structural topology optimization. *Computer methods in applied mechanics and engineering* 192, 1-2 (2003), 227–246.

Joshua Wolper, Yu Fang, Minchen Li, Jiecong Lu, Ming Gao, and Chenfanfu Jiang. 2019. CD-MPM: Continuum damage material point methods for dynamic fracture animation. *ACM Transactions on Graphics (TOG)* 38, 4 (2019), 119.

Weisheng Zhang, Jian Zhang, and Xu Guo. 2016. Lagrangian description based topology

optimization—a revival of shape optimization. *Journal of Applied Mechanics* 83, 4 (2016), 041010.